Simo A. Nurmi

COMPUTATIONAL AND EXPERIMENTAL INVESTIGATION OF THE GROOVED ROLL IN PAPER MACHINE ENVIRONMENT

Thesis for the degree of Doctor of Science (Technology) to be presented with due permission for public examination and criticism in Auditorium 1382 at Lappeenranta University of Technology, Lappeenranta, Finland, on the 16th of December 2009, at noon.

Acta Universitatis
Lappeenrantaensis
379

Supervisor Professor Jari Backman
LUT Energy
Lappeenranta University of Technology
Finland

Reviewers Professor Fritz Bark
KTH Mechanics
KTH Royal Institute of Technology
Sweden

Professor Hiromu Hashimoto
Department of Mechanical Engineering
Tokai University
Japan

Opponents Professor Fritz Bark
KTH Mechanics
KTH Royal Institute of Technology
Sweden

Professor Jari Hämäläinen
Department of Physics
University of Kuopio
Finland

ISBN 978-952-214-890-2
ISBN 978-952-214-891-9 (PDF)
ISSN 1456-4491

Lappeenrannan teknillinen yliopisto
Digipaino 2009

To my family

ABSTRACT

Simo A. Nurmi

Computational and Experimental Investigation of the Grooved Roll in Paper Machine Environment

Lappeenranta 2009
100 Pages
Acta Universitatis Lappeenrantaensis 379
Diss. Lappeenranta University of Technology
ISBN 978-952-214-890-2, ISBN 978-952-214-891-9 (pdf), ISSN 1456-4491

In the paper machine, it is not a desired feature for the boundary layer flows in the fabric and the roll surfaces to travel into the closing nips, creating overpressure. In this thesis, the aerodynamic behavior of the grooved roll and smooth rolls is compared in order to understand the nip flow phenomena, which is the main reason why vacuum and grooved roll constructions are designed. A common method to remove the boundary layer flow from the closing nip is to use the vacuum roll construction. The downside of the use of vacuum rolls is high operational costs due to pressure losses in the vacuum roll shell. The deep grooved roll has the same goal, to create a pressure difference over the paper web and keep the paper attached to the roll or fabric surface in the drying pocket of the paper machine. A literature review revealed that the aerodynamic functionality of the grooved roll is not very well known. In this thesis, the aerodynamic functionality of the grooved roll in interaction with a permeable or impermeable wall is studied by varying the groove properties.

Computational fluid dynamics simulations are utilized as the research tool. The simulations have been performed with commercial fluid dynamics software, ANSYS Fluent. Simulation results made with 3- and 2-dimensional fluid dynamics models are compared to laboratory scale measurements. The measurements have been made with a grooved roll simulator designed for the research. The variables in the comparison are the paper or fabric wrap angle, surface velocities, groove geometry and wall permeability. Present-day computational and modeling resources limit grooved roll fluid dynamics simulations in the paper machine scale. Based on the analysis of the aerodynamic functionality of the grooved roll, a grooved roll simulation tool is proposed.

The smooth roll simulations show that the closing nip pressure does not depend on the length of boundary layer development. The surface velocity increase affects the pressure distribution in the closing and opening nips. The 3D grooved roll model reveals the aerodynamic functionality of the grooved roll. With the optimal groove size it is possible to avoid closing nip overpressure and keep the web attached to the fabric surface in the area of the wrap angle. The groove flow friction and minor losses play a different role when the wrap angle is changed.

The proposed 2D grooved roll simulation tool is able to replicate the grooved aerodynamic behavior with reasonable accuracy. A small wrap angle predicts the pressure distribution correctly with the chosen approach for calculating the groove friction losses. With a large wrap angle, the groove friction loss shows too large pressure gradients, and the way of calculating the air flow friction losses in the groove has to be reconsidered.

The aerodynamic functionality of the grooved roll is based on minor and viscous losses in the closing and opening nips as well as in the grooves. The proposed 2D grooved roll model is

a simplification in order to reduce computational and modeling efforts. The simulation tool makes it possible to simulate complex paper machine constructions in the paper machine scale. In order to use the grooved roll as a replacement for the vacuum roll, the grooved roll properties have to be considered on the basis of the web handling application.

Keywords: Grooved roll, smooth roll, fabrics, CFD, web handling, paper machine

UDC: 676.056.4 : 621.771.074

ACKNOWLEDGEMENTS

I thank my supervisor professor Jari Backman for his support during my research work.

I am grateful for the reviewers, Professor Fritz Bark from KTH Royal Institute of Technology and Professor Hiromu Hashimoto from Tokai University, for their comments and suggestions during the review process.

It is an honor for me to thank Dr Kari Juppi and Dr Lars Martinsson for their support during the grooved roll project. This thesis would not have been possible without the financial support of Albany International, The Finnish Funding Agency for Technology and Innovation (TEKES) and Metso Paper.

Very many thanks to managing director Kenneth Eriksson of Process Flow Ltd Oy for providing the work facilities and the needed computational power for the computational fluid dynamics simulations.

I also thank Dr Juha Leimu and his research team at Turku University of Applied Sciences for performing the measurements with the grooved roll simulator.

Special thanks to all of my colleagues for supporting me during the research, especially M.Sc Fredrik Bergström, Lic.Tech David Hammarström and Dr Eero Immonen, for reviewing and commenting on the thesis.

My sincerest thanks to my parents, brothers, sister and my parents-in-law for their understanding and support.

Finally, I owe my deepest gratitude to my wife Armi and my son Aleksi for their loving support during the long project.

Turku, December 2009

Simo Nurmi

CONTENTS

ABSTRACT **5**
ACKNOWLEDGEMENTS **7**
CONTENTS **9**
NOMENCLATURE **11**
1 Introduction **15**
1.1 Historical outline 17
1.2 Motivation 18
1.3 Objectives 21
1.4 Previous studies 23
2 Model development **29**
2.1 Smooth roll 29
2.1.1 Air flows in nip areas 29
2.1.2 Closing nip 31
2.1.3 Opening nip 35
2.1.4 Static pressure at the closing and opening nips 37
2.2 3D grooved roll 39
2.2.1 Flow losses due to entrance and exit 41
2.2.2 Flow friction losses in the groove 43
2.2.3 Simulation results of the 3D grooved roll 44
2.3 2D grooved roll simulation tool 46
2.3.1 Simulation results of the 2D grooved roll model 48
2.3.2 Solution strategy for 2D grooved roll simulations 52
2.3.3 Fabric model 53
2.4 Computational fluid dynamics 55
2.4.1 Convergence 56
2.4.2 Uncertainties due to discretization 59
3 Model validation **61**
3.1 Experimental setup 61
3.1.1 Simulator geometry 61
3.1.2 Groove pressure measurement 63
3.1.3 Measurement procedure 65
3.1.4 CFD models 65
3.1.5 Test cases 66
3.2 Results 67
3.2.1 Groove aerodynamic functionality 68

3.2.2 3D grooved roll model vs. 2D GRT model 73
3.2.3 Comparison of the 3D grooved roll model and measurements 78
3.2.4 Considerations on pressure measurements techniques 82
3.3 Measurement uncertainty 85
4 Discussion 87
5 Conclusions 91
REFERENCES 93
APPENDIX A 99
APPENDIX B 100

NOMENCLATURE

2D	2-dimensional
3D	3-dimensional
A	area [m²]
C	inertia loss term [kg/m^4]
C_{2D}	porous-jump coefficient [1/m]
D	viscous loss term [kg/m³s]
d	diameter [m]
E	relative uncertainty [%]
f	friction coefficient [-], force per volume [N/m³]
G	groove fraction [-]
g	gravity [m/s²]
h	nip gap [mm]
it	iteration [pcs]
K	minor loss coefficient [-]
L	length [m], boundary layer development length [m]
m	thickness [m]
N	cell count [pcs], resolution
p	pressure [Pa]
Q	resolution threshold
Re	Reynolds number [-]
r	radius [m]
S	source term [N/m³]
s	groove length in tangential direction [m], length [m]
U	velocity component in x-direction [m/s], voltage [V]
V	volume flow proportion [-], velocity component in y-direction [m/s]
v	velocity [m/s]
W	velocity component in z-direction [m/s]
$\dot{V}$	volume flow [m³/s]
v	velocity [m/s]
x	x-coordinate [m]

y	y-coordinate [m]
z	horizontal elevation [m]

Greek

α	angle [deg], permeability [m^3/h m²]
β	angle [deg]
ε	uncertainty
ρ	density [kg/m³]
ω	angular velocity [rad/s]
v	kinematic viscosity [m²/s]
μ	viscosity [kg/ms]

Superscripts

‘	total
*	modified, dimensionless

Subscripts

0	initial
1	tangent point, radial component
2D	2-dimensional
a	atmospheric, air
accs	acceleration sensitivity
adc	analog to digital converter
amp	strain gage amplifier
c	circumferential
e	emptying, entrainment, opening nip
eva	excitation voltage accuracy
evd	excitation voltage drift
ef	effective
eff	effective
exp	experimental
f	fine, filling, fraction
fs	full scale
g	groove

h	height, hydraulic
in	closing nip
l	roll land
lam	laminar
nlh	combined non-linearity and hysteresis
ps	pressure sensor
rad	radial
rel	relative
ref	reference
s	groove tangential direction
t	total
tzs	thermal zero shift
tss	thermal sensitivity shift
turb	turbulent
w	width
wall	wall
wrap	wrap angle
visc	viscous
vd	dynamic pressure
x	x-direction

Abbreviations

A/D	Analog to Digital
CFD	Computational Fluid Dynamics
GCI	Grid Convergence Method
GRT	Grooved Roll Simulation Tool
FSI	Fluid Structure Interaction
LDV	Laser-Doppler Velocimeter
PC	Personal Computer
RE	Richardson Extrapolation method
RNG	Renormalization Group theory
TUAS	Turku University of Applied Sciences

1 INTRODUCTION

In this thesis, the main interest is in grooved rolls and their functionality in the paper machine environment. Rolls are widely used in paper machines to heat, press and support paper webs and fabrics, in order to facilitate rapid drying and transport of the paper web through the machine. The roll surfaces can be smooth, as shown in Figure 1*b*, or they can be rough, for example *grooved* and *drilled.* A combination of a grooved and drilled roll is called a *vacuum roll,* shown in Figure 6*b*. A roll with deep grooves on its surface is called a *grooved roll*. The purpose of the different surface coatings and textures is to improve the web handling in paper making and to save energy. A grooved roll is shown in Figure 1*a*.

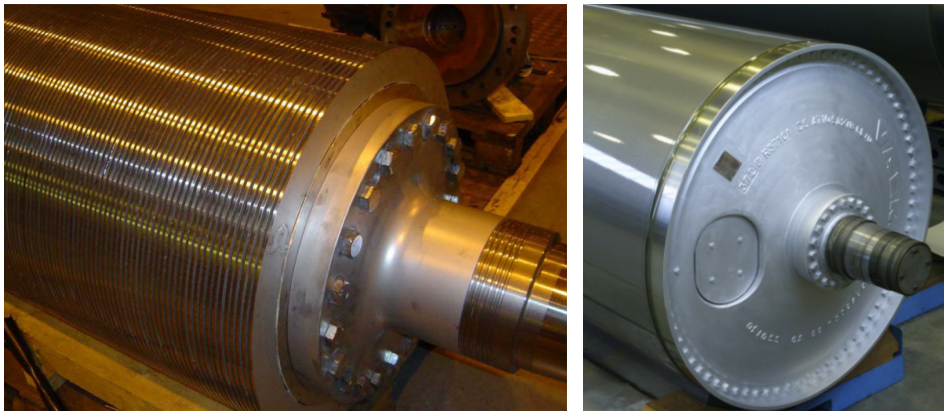

Figure 1: *a)* A roll with deep grooves [22], *b)* A roll with smooth surface [31]

Grooved and vacuum rolls are web handling devices. Web handling refers to the controlling of manufacturing processes where the main raw material is a continuous flexible membrane called a *web*. Examples of industrial processes involving web handling include paper or plastic in the printing industry, cardboard in the packaging industry, rolled steel slabs of continuous steel in the steel industry, and previously, magnetic tape in the recording industry. The web motion in a web handling device is significantly influenced by the air flow.

Vacuum roll and grooved roll constructions are used in the drying section of the paper machine to improve *runnability*. Runnability is related to web transfer, where unexpected web deformations and web flutter may occur [19]. There are several factors that affect runnability, such as the strength properties of the web, and the raw materials [19]. The components and processes of the paper machine, such as grooved rolls, vacuum rolls and pressing, affect the runnability factors [19].

Rolls with low grooves are typically used in the drying section and in the reel. Rolls with deep grooves installed in the paper machine drying section have been studied by Kurki & Martikainen [22]. In drying section configurations, both the vacuum and grooved rolls are partly covered with drying fabrics. A schematic view of the paper machine is shown in Figure 2.

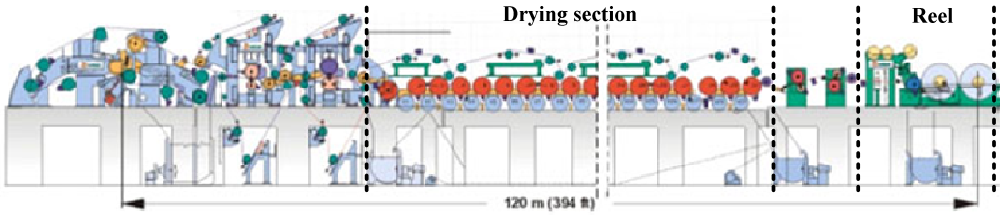

Figure 2: Schematic view of the paper machine [16].

The complexity of the paper machine construction and the fluid flows in the paper machine are obvious: the flow types vary from single phase to multiphase flows; the rolls and fabrics, together with paper web, moving with high velocity, create a challenge for improving the efficiency of the paper machine. The largest paper machines today are over 11 m wide, with the design speed over 2000 m/min. A modern paper machine is shown in Figure 3. The components of a paper machine can be designed with the help of *computational fluid dynamics* (CFD) simulations. This approach lowers the design costs and potentially raises the energy efficiency of the machine. So called virtual prototypes can be tested beforehand with CFD, and thus expensive pilot machine experiments and the time to market can be minimized.

Figure 3: The modern paper machine [16].

Developing the boundary layer flows at webs, fabrics and roll surfaces traveling towards a narrowing area of the rotating roll and moving surface, called a *nip*, creates air flows and air pressures which are not desirable from the web handling perspective. The term *wrap angle* refers to the roll surface covered with the web or the fabric. In Figure 4, the opening nip is shown with number 1 and closing nips with 2 and 4. These problematic areas are the main topic of this work.

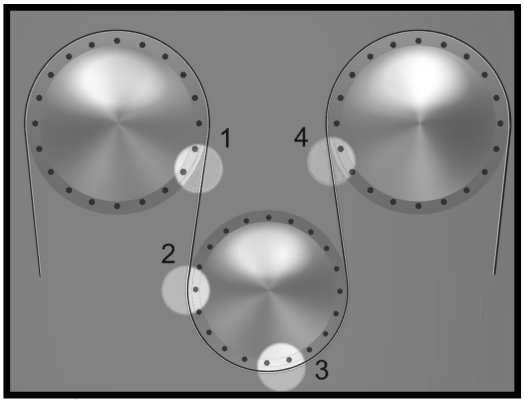

Figure 4: Dryer group with nips [31].

In this thesis, computational fluid dynamics simulations are utilized in the analysis of grooved rolls in the papermaking environment. Present-day computational and modeling resources limit detailed paper machine scale 3-dimensional simulations; therefore a 2-dimensional simulation tool for grooved roll needs to be developed. The *grooved roll simulation tool* (GRT) describes the aerodynamic features of the grooved roll for a large scale paper machine simulation model with the help of porous media. A comparison of some aerodynamic properties between smooth and grooved rolls is made in this thesis. The grooved roll simulation models are validated with laboratory scale measurements.

1.1 *Historical outline*

During the development of paper machines, the demand for higher speed (> 900 m/min) led to the invention of a single-felted dryer group construction, introduced in 1976 [15]. Vacuum rolls were introduced in 1985 first by Beloit with a small diameter roll where the vacuum zone affected the fabric coverage [15]. The second was Valmet in 1985 with a larger diameter roll and high velocity blow-box [15]. According to Juppi [15], this construction was called the

Uno-Run. The vacuum roll is a widely used component in paper machines, although during the years, modifications to blow-boxes and vacuum rolls have been done. Juppi [15] suggests a new vacuum roll construction with two vacuum chambers.

The earliest record of a grooved roll found by the author of this thesis is Brafford's [2] invention in 1971, where micro-grooves were introduced. The micro-grooved roll was intended to be used in the forming section of the paper machine to eliminate opening nip underpressure. A grooved roll with deep grooves was introduced in 2005 by Kurki & Martikainen [23, 24]. This type of grooved roll is studied in this thesis.

Computational fluid dynamics is used as a tool to study fluid flows in web handling devices. In the area of paper machinery, there are many examples of studies where CFD analysis has been successfully utilized. Karlsson [18] used CFD in 1989 to solve the airflows in the paper machine drying pocket, and so did Pakarinen et al. [41]. Zagar [48] simulated in 1996 the air flotation dryer in order to understand web stability phenomena. Widlund et al. [51] compared results obtained by laser-doppler velocimetry (LDV) and CFD results in the paper machine dryer section. In 2001, Juppi [15] and Laakkonen [27] used CFD to analyze the dryer pocket. Multi-physics simulations, such as fluid structure interaction (FSI) are becoming more common [13].

1.2 *Motivation*

Runnability and energy consumption are important factors when considering improvements to the paper machine construction. In modern high speed paper machines, the interaction of boundary layer flows on the rolls, fabrics and paper web often results in an undesirable pressure development at nip regions, ultimately causing an uncontrolled motion of the paper web, i.e. runnability problems [7, 19, 28, 41]. Figure 5 shows problematic areas with overpressure and negative pressure caused by boundary layer flows at the paper and fabric surfaces.

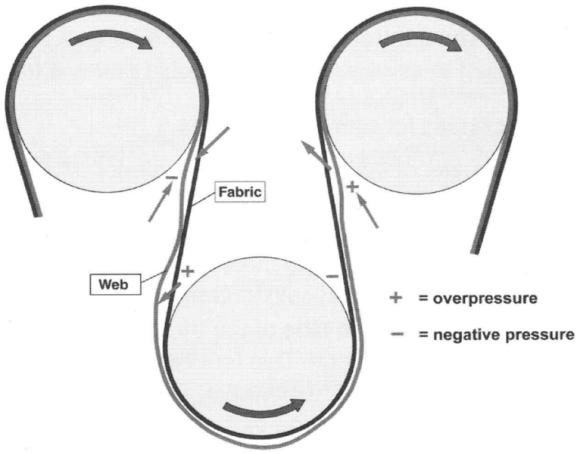

Figure 5: Runnability problems in a dryer group [19, 7].

The runnability issue can be mitigated by using the so-called *vacuum roll* construction and a *high velocity blow-box,* namely *Uno-Run* [19]. The vacuum roll and blow-box create the required pressure profile over the paper web at the opening and closing nips of the drying section of the paper machine. The surface of the vacuum roll is grooved with low grooves, and the groove bottoms are perforated (see Figure 6*b*) [19, 42]. Suction through the roll removes the excess air from the closing nip, improving the runnability. A high velocity blow-box, on the other hand, increases the underpressure within the pocket area, keeping the paper attached to the fabric. In Figure 6*a*, a basic single-run dryer group is shown.

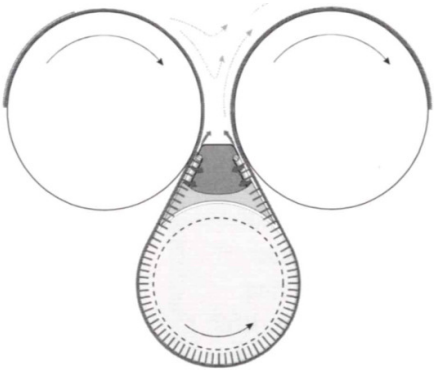

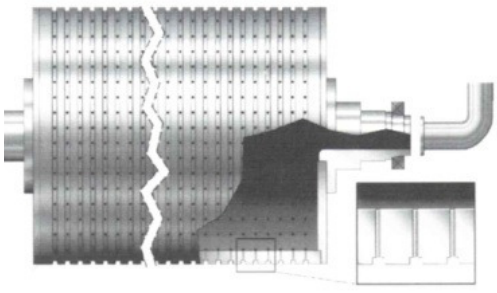

Figure 6: *a)* Single-run dryer group with a vacuum roll and a high-velocity blow box between the two drying cylinders [19], *b)* A vacuum roll [19].

A significant drawback of the vacuum roll construction is its high operational cost, caused by the production of suction air for the vacuum roll. The need for energy efficiency raises the question of whether there is a way to improve the vacuum roll construction by changing its aerodynamic functionality. Juppi suggests a new vacuum roll construction where suction is divided in two adjustable sections [15]. The third section is located in the open area blocked with a seal to prevent the ambient air from flowing into the vacuum roll [15]. The results show that the construction improves the runnability in high speed paper machines [15]. A downside of the construction is the need for higher underpressure and more complicated construction compared to The Uno-Run single-run dryer group.

The grooved rolls introduced by Kurki & Martikainen [22] may be a replacement for the widely used vacuum rolls in improving the runnability and lowering the energy consumption in high speed paper machines. The vacuum and grooved rolls have the same goal, to create a pressure difference over the web to keep the web attached to the fabric surface. The difference in the function principle is how the underpressure is created. The vacuum roll needs an external fan and ducts to remove the air from the suction roll. The grooved roll creates underpressure to grooves without any external fan [22]. The grooved roll construction in the dryer group needs modifications in the blow-box as well, which is not included in this research.

Changing the vacuum rolls to grooved rolls in the paper machine will save energy. The vacuum roll shell pressure loss is 2000 Pa, and the volume flow through the roll shell is 800m³/h per meter of machine width [19]. Assuming that the same amount of air is moved from the drying pocket as the vacuum roll moves, the energy saving is approximately 0.45kW per meter of paper machine width. In a present-day high capacity paper machine with thirty grooved rolls, paper width of eleven meters and running time 7200 hours, the energy saving is 1080 MWh. The changes in the fan efficiency due to smaller pressure increase have not been considered.

How does a grooved roll work and what are its important parameters? What is the optimal groove size? Research around the aerodynamic functionality of rolls with deep grooves is not abundant. 3D CFD simulations of grooved rolls in large paper machine sections are not feasible with present-day computational or modeling resources. In order to avoid detailed 3D modeling of the groove, a reasonably simplified model is needed. Such a

model would provide a means to study the grooved rolls in large and complicated geometries based on actual paper machine sections. New grooved roll applications could be created with the help of the new model. Furthermore, benefits for product development can be obtained by using numerical simulations. In other words, this means fewer prototypes and faster product development cycles with a smaller financial budget. From the measurement point of view, phenomena that cannot be measured can be seen with computational models of the paper machine.

1.3 *Objectives*

The research work presented in this thesis is focused on studying the aerodynamic functionality of the deep grooved roll interacting with an impermeable wall with a small and a large wrap angle. A comparison with a smooth roll is made. The t*ail threading* condition where the grooved roll and a permeable wall, namely fabric, interact with each other with a large wrap angle is studied as well. The roll radius, groove size, rotation speed, boundary layer flow development length, fabric permeability, and wrap angle are important variables. Air velocities, as well as the pressure in the grooves and nip areas are also studied, in order to understand how the grooved roll works. The opening and closing nips are studied with the help of smooth roll models.

Computational fluid dynamics (CFD) simulations are used as the research tool. 3D CFD simulations of grooved rolls in large paper machine sections are not feasible with present-day computational or modeling resources. A reasonably simplified 2D grooved roll CFD model, with a *grooved roll simulation tool* (GRT), is developed. The grooved roll simulation tool is able to capture the *minor losses* and the friction flow losses similarly to a 3D grooved roll CFD model. In this case minor losses refer to the pipe flow terminology, for example flow losses due to sudden expansions and contractions or pipe entrance and exit [50].

The simulation results with the groove roll simulation tool and 3D grooved roll CFD models are validated with laboratory scale measurements. The grooved roll measurement setup includes the conditions where the grooved roll is partly covered with a permeable drying fabric or an impermeable smooth surface. The wrap angle is 180 degrees.

This thesis offers new knowledge:

- for understanding the physical phenomena that govern the operation of grooved rolls,

- by developing a grooved roll simulation tool for simulating complex grooved roll constructions with present-day computational and modeling resources.

The grooved roll simulation tool does not include FSI, or heat and mass transfer simulations. The used fabric models are based on the work of Laakkonen [26]. The cross-directional air flows cannot be solved with the grooved roll simulation tool. In future development work, expansion of the grooved roll simulation tool to a full 3D grooved roll CFD model including side leakage and cross-directional air flows will be in focus.

The author of this thesis has derived the presented equations, conducted and analyzed the results of the numerical simulations, and analyzed the measurement data. The laboratory scale measurements have been done by Dr J. Leimu and his staff at Turku University of Applied Sciences (TUAS) in summer and autumn 2009.

The thesis is divided to five main chapters: introduction, model development, model validation, discussion and conclusions. Introduction provides insights into previous studies made in this research area, as well as argumentation on why the work has been done. The second chapter, model development, describes the smooth and grooved roll aerodynamic functionality and the theory behind it. CFD simulation results are compared to analytical solutions. The third part is model validation, focusing on measurements and CFD model validation. The last two chapters, discussion and conclusions are final remarks.

Two conference papers have been written during the groove roll project: *"Comparison of aerodynamics between a smooth and grooved roll interacting with a rigid impermeable horizontal wall"*[38] and *"Modeling grooved rolls with moving 2D porous media"* [39]. M.Sc Simo Nurmi, the corresponding author of these papers, was in charge of the preparation of the papers and conducting the numerical simulations. Revisions of the conference papers were made with the help of M.Sc F. Bergström, Dr E. Immonen, Dr A. Lehtinen, Dr K. Juppi and Dr L. Martinsson. Besides the results of reported in the above conference papers, this thesis contains work by the author that has not been published earlier. The laboratory scale measurements have been done by Dr J. Leimu and his staff at Turku University of Applied Sciences (TUAS) in summer and autumn 2009. This research supports other research approaches, such as heat transfer and fluid structure interaction.

1.4 *Previous studies*

There are several different research approaches in the area of web handling: winding, nip mechanics, web tension control, air entrainment, and friction, among others. When considering fluid mechanics in the interaction of rolls and moving surfaces, the starting point is the boundary layer flows. The boundary layer flows create overpressure in the closing nips, which might detach the web from the roll or the fabric surface. In the worst case this will lead to loss of traction between the web and the roll, wrinkling, or to web breaks. In the field of paper machine research, an overview on boundary layer flows can be found in Juppi's [15] thesis. Simulations and measurements of the boundary layer flow and flow through the permeable fabric with rough fabric surfaces are the basis of Laakkonen's [26] work.

Laakkonen [25, 26, 27] has developed a large scale fabric model based on small scale simulations with actual fabric geometry. The model uses the moving porous media approach to characterize important fabric properties in a large scale paper machine model [26]. Measurements were made in a wind tunnel in order to validate the developed model. In the present thesis, Laakkonen's fabric model is used to simulate the permeable wall, especially the tail threading condition.

An analytical solution for the pressure development in the closing nip region with a smooth roll can be found in a study of Karlsson [18]. The model assumes that the boundary layer flows from the web and roll surface create an impulse force to the closing nip when the air flow speed is decelerated to zero. Karlsson applies kinematic terms of Navier-Stokes equations. Air entrainment between the roll and the moving wall is excluded from Karlsson's study. His results have been later used by Juppi [15] and Kurki [21]. Kurki [21] considers also the viscous pressure term in the closing nip derived from Navier-Stokes equations, shown in Equation 1 [21].

$$p_{visc} = \frac{16 \rho_a \nu_a v_x r^2}{x^3} \tag{1}$$

In Figure 7, the static pressure is schematically presented as a function of distance from the nip contact point. The kinematic and viscous pressure development is now taken into account. Viscous pressure development affects in the area close to the contact point where the flow is laminar [21]. Kurki [21] points out that pressure levels lead to infinite at the contact

point, which is not possible in real systems, due to the paper permeability, air entrainment and air flows to the cross direction.

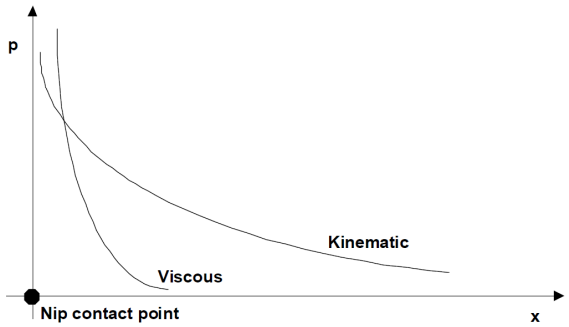

Figure 7: Viscous and kinematic pressure development at the closing nip [21].

Opening nip air flow properties have been studied in [21] and [30]. Kurki [21] has derived an equation for the opening nip pressure behavior as a function of roll radius, web velocity and distance from the nip. He assumes that the flow is a laminar Couette flow with a parabolic velocity profile without air leakage to the nip. This analytical solution leads to unrealistic pressure profiles because of the idealized assumption. Widlund et al. [51] have measured and simulated with CFD, dryer cylinder opening nip velocity profiles with dryer fabric and paper. Their results show clearly that the outflows from the nip are caused by the developing boundary layer flows, and the inflow fills the opening nip underpressure. Measurement results of the cylinder and dryer fabric opening nip are shown in Figure 8 [51]. The highest inflow is measured with coated dense fabric with low permeability.

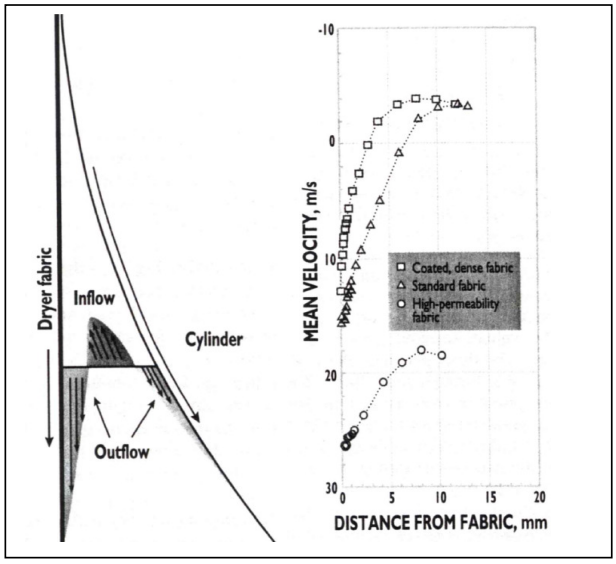

Figure 8: Air flow at opening nip presented with velocity vectors [51].

Leimu [30] used computational fluid dynamics to simulate the opening nip in order to get quantitative values for the pressure. Compressible and incompressible models were tested, as well as air leakage in the nip. Air entrainment between the rotating roll and the web affects the traction, as well as the air leakage to the opening nip with a small wrap angle. In the present thesis, solutions for aerodynamic properties in a closing and opening nip are coupled and solved with CFD simulations.

In real web handling configurations, the web deformation and interaction with the surrounding air in the closing and opening nip have an important role. The estimation of web deformations is becoming more common in web handling. Runnability issues, such as web flutter [17, 46], air entrainment [5], and wrinkling [9] can be simulated by using fluid-structure interaction (FSI) simulation. Nurmi et al. [40] have simulated web flotation and aerodynamic instabilities in a flotation dryer. The goal was to develop a model to predict the propagation of stress waves in a viscoelastic thin web. Müftü has studied the mechanics of thin, flexible, translating media from different viewpoints by using FSI [33, 34, 37]. Kurki [21] and Kurki & Åkerholm [23] have also developed FSI-simulation tools and methods for paper machine environments. Kurki's web model is nonlinear, covering the web flutter and tension modeling in long free draws. The most recent FSI-tool, presented by Immonen et al. [13, 14], solves the paper and fabric deflections separately in cases where the web is

supported by the fabric. Displacements are calculated based on the local pressure differences, gravity, adhesion, and centrifugal forces, and on a given set of boundary conditions [14]. In the model of Immonen et al., the tension can be different in the web and the fabric. The FSI-tool has been built for a commercial CFD solver and it can be used in complex and modern single-run paper machine drying section simulations [14]. Leimu has studied the opening nip web deformation with an element model by changing the web tension and adhesion between the web and the drying cylinder [29, 30]. The model is validated with experiments. In the present thesis, FSI simulations are not discussed, they are presented here to remind of the complexity of web handling problems as a future challenge.

Air entrainment in winding, as well as between the roll and moving wall, has been studied by various researchers. Hashimoto has derived an equation for the air film thickness between the web and the roll by using the finite width compressible foil bearing theory [11]. The entrained air lowers the traction between the roll and the web. A review of air entrainment and traction can be found in [45] and [32]. The gap throttle effect has been introduced by Welp et al. [53] [54] as an application to prevent air entrainment to the closing nips of rolls. The gap throttle effect is created with a small stationary foil construction located in the closing nip. The functionality of the foil is based on the viscous losses affected by the stationary wall [54]. In winding applications, the gap throttle foil stabilizes the web, allows higher winding speed, and increases the radial tension in the wound rolls [54].

Side leakage and permeable web are factors increasing the traction by allowing the entrained air to escape. Web permeability has been studied by Ducotey & Good [5] and Hashimoto & Okajima [10]. They conclude that permeability decreases the air film thickness. A comparison between measurements and the developed models show that the agreement is reasonable. Müftü & Altan [36] have introduced a steady-state air lubrication model with a permeable web moving over cylindrical guide. Their model seems to work only with very high fiber fractions [36].

Another approach to increase the traction is to use circumferential micro grooves on the roll surface. In this case, the entrained air flows into the groove and the asperity contact increases, which can be seen as increased traction [6]. The groove height is typically 100-200 µm in applications improving traction [6, 9]. The latest study of Hashimoto & Hikita [9] shows the importance of tension control and the roll micro-grooves in reducing web slippage

and wrinkling. In the winding of the web, grooved rolls are used to prevent air bags in the wound rolls by letting the entrained air pass through the nip [44]. Figure 9 shows the main function principle in the winding applications for the so called *venta-groove* and shallow groove [44]. In the venta-groove, the web does not bend into the groove, which may lead to a ballooning effect with the web in the wound roll [44].

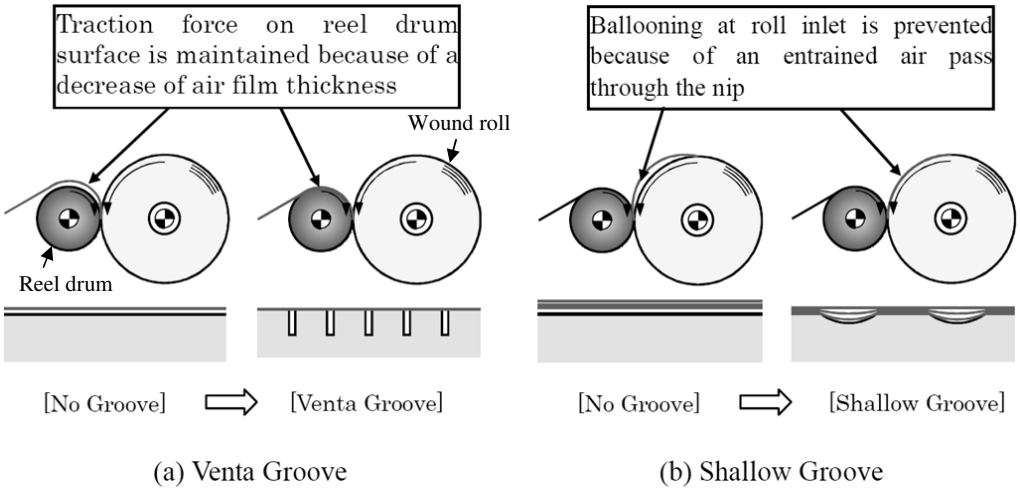

Figure 9: The effect of reel drum grooving in winding [44].

A roll with deep grooves, shown in Figure 1a, has been introduced by Kurki and Martikainen in 2005 [22]. Their article presents insights into how grooved rolls can under-pressurize the grooves and thus improve the runnability in a single-run dryer group. Measurements with a pilot machine and CFD are compared to each other. According to Kurki & Martikainen, the pressure development follows adaptively the Bernoulli equation, which does not include minor or viscous flow losses.

From the numerical modeling point of view, the paper drying models introduced by Bergström et al. [1] and Lehtinen et al. [28] can be used to evaluate different dryer group constructions, including a 2D grooved roll model. The models have been developed to be product development tools to enhance paper drying. Both models calculate the heat and mass transfer in paper and between paper surfaces. In the present thesis, heat and mass transfer are not considered as variables. In future grooved roll development work, heat and mass transfer will be considered as model features.

2 MODEL DEVELOPMENT

Rotating rolls and moving surfaces create boundary layer flows, which is an important factor when considering the aerodynamics of smooth or grooved rolls. It is important to be able to control the boundary layer flows with web handling applications. In Section 2.1, a smooth roll interacting with an impermeable horizontal wall is analyzed by means of theoretical and computational fluid dynamics approaches. The closing and opening nips of the smooth rolls, as well as the pressure development in the nips are discussed in separate subsections.

In Section 2.2, grooved rolls are introduced. The functionality of the grooved roll is studied in order to understand the factors affecting the aerodynamics of the roll. A simulation tool which enables simulating the grooved roll in the paper machine scale is introduced in Section 2.3. In real life, paper webs or paper machine fabrics are not impermeable. Therefore, a grooved roll interacting with permeable fabric is considered as well. The permeable fabric is simulated with the method introduced by Laakkonen [25].

Section 2.4 includes a short description of applied computational fluid dynamics and analysis of the convergence and numerical accuracy.

2.1 *Smooth roll*

2.1.1 Air flows in nip areas

Moving walls and rotating rolls develop boundary layer flows on their surfaces. When the flows approach the nip area, the flow reverses its direction partly, creating backflow and increasing the static pressure at the closing nip. At the opening nip, the boundary layer flows start to develop on the surfaces and transport air away from the nip, creating underpressure. This underpressure causes inflow into the opening nip. The air flow opposite the boundary layer flows is defined as backflow in the closing nip and inflow in the opening nip. From the web handling point of view, high over- and underpressures in the nip areas are not desirable.

Analytical and computational models with smooth rolls are presented in the following two chapters. The examined properties are pressure development comparison, and the flow direction and velocity profiles in the closing and opening nips. In Figure 10, the air flow behavior, as well as the turbulent and laminar flow areas at the closing and opening nips is shown schematically [21].

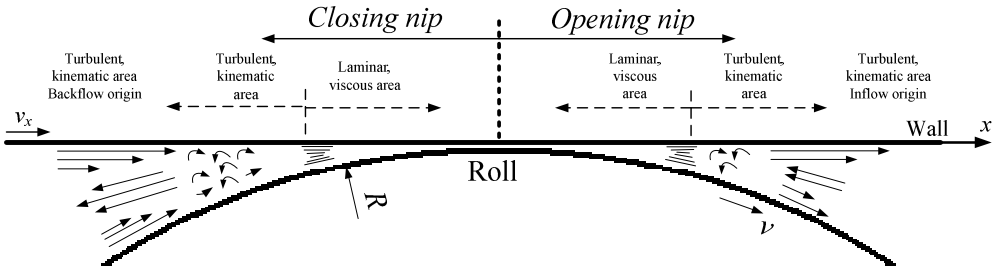

Figure 10: Air flow at closing and opening nip, redrawn from [21].

A simple CFD model, shown in Figure 11, has been created to present velocity profiles and flow behavior in the closing and opening nips. The model consists of a horizontal wall with boundary layer development length *L* and rotating cylinder with radius *R,* The velocity profiles are shown in Sections 2.1.2 for the closing nips and in 2.1.3 for the opening nips. In the CFD model, the boundary layer development length has been chosen to be 1, 2 and 3m. A vertical wall is placed on the left hand side of the roll in order to eliminate disturbances and to reset the boundary layer flow. This model is assumed to be infinitely wide (2D), and thus side leakage is not included. The surfaces are hydraulically smooth and impermeable. The tension in the wall is assumed to be infinite; therefore the wall shape does not change when the wall travels past the roll. The pressure inlet boundary condition is set in the left, right and bottom boundaries with turbulent kinetic energy 1 m^2/s^2 and turbulent dissipation rate 1 m^2/s^3 values. The model is shown with nomenclature in Figure 11. Number 1 shows the places where the boundary layers start to grow, and number 2 is the closing nip region where the boundary layer flows collide.

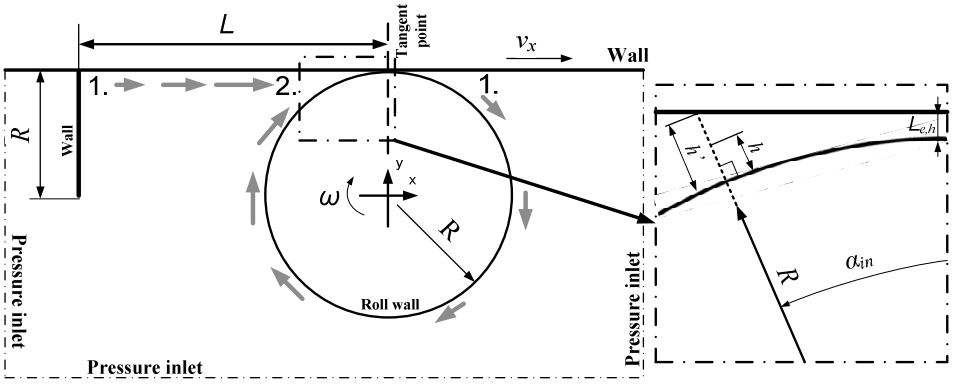

Figure 11: Boundary layer development in the case of a moving horizontal wall and smooth roll, with nomenclature.

For the evaluation of the velocity profile, the dimensionless nip gap h^* is shown in Figure 11 and defined in Equation (2)

$$h^* = \frac{h}{h'}, \tag{2}$$

where h is the distance from the roll wall perpendicular to the direction of the horizontal wall, and h' is the total length of the nip gap. On the roll wall h^* is 0 and at the fabric surface h^* is 1. The velocity profiles are captured from the opening and closing nips. The angle α is 0° at the tangent point and starts to increase on both sides of the opening or the closing nip. $L_{e,h}$ is the constant air entrainment height, chosen to be 100 µm based on air entrainment studies, and it is used for all smooth roll CFD models.

Turbulence in the nip gap is an interesting issue. The air flow in the nip area can be modeled as flow between two convergent plates. The hydraulic diameter d_h is then twice the distance between the plates. In the present case d_h has been chosen to be $2h'$. In the pipe flows, the main flow direction is usually unidirectional. In the closing nip area there are bi-directional flows, boundary layer flows and backflow. In the opening nip, the boundary layer flows start to develop from the nip, and inflow fulfills the nip underpressure (see Figure 10). The absolute value of the tangential velocity v_t along the h^* path line is used in the calculation of the Reynolds number Re shown in Equation (3)

$$\mathrm{Re} = \frac{\rho_a |v_t| 2h'}{\mu_a}, \tag{3}$$

where ρ_a is air density and μ_a is air viscosity.

2.1.2 Closing nip

An analytic solution for the closing nip pressure is shown in Equation (4) [18]

$$p(\alpha_{in}) = 0.8 p_{vd}\left[0.5 \ln\left(10\, c_{ef}\frac{L}{r}\right) - \ln(\alpha_{in})\right], \tag{4}$$

where $p_{vd} = 0.5\rho_a v_x^2$, α_{in} is the angle from tangent point away from the closing nip, c_{ef} is the skin friction coefficient, L is the boundary layer development length, r is the roll radius, v_x is surface velocity, and ρ_a is air density. A derivation of the equation (4) can be found in [18]. Karlsson [18] assumes that the boundary layer flows are decelerated in the closing nip, and

that an impulse force creates the pressure. In another words, backflow from the closing nip is not considered. Air is not allowed to flow from the closing nip through the tangent point to the opening nip in the analytic solution. Note that as $\alpha \to 0$, $p(\alpha) \to \infty$, which is unrealistic. A comparison of static pressure curves of the analytical and CFD models is presented in Section 2.1.4.

The air flow simulation with the CFD model of the closing nip with a smooth roll and a horizontal wall described in Section 2.1.1, reveals similar aerodynamic behavior as shown in Figure 10. In the geometry used, the roll radius r is constant R, whereas the wall and roll surface velocity v_x and boundary layer development length L are variables.

In Figure 12*a*, the surface velocity v_x is 1500 m/min and L is 3 m. The velocity profiles from the closing nip gap shows that the backflow starts from the area between 3° and 4° where tangential velocity v_t is smaller than zero. This area is named as backflow origin. Figure 12*b* illustrates that the backflow becomes stronger when the surface velocities are increased. The variation in tangential velocity is between -2 to -4.7 m/s. In the closing nip velocity profiles, the negative tangential velocity sign designates the backflow direction. This phenomenon is shown in Figure 12*b*.

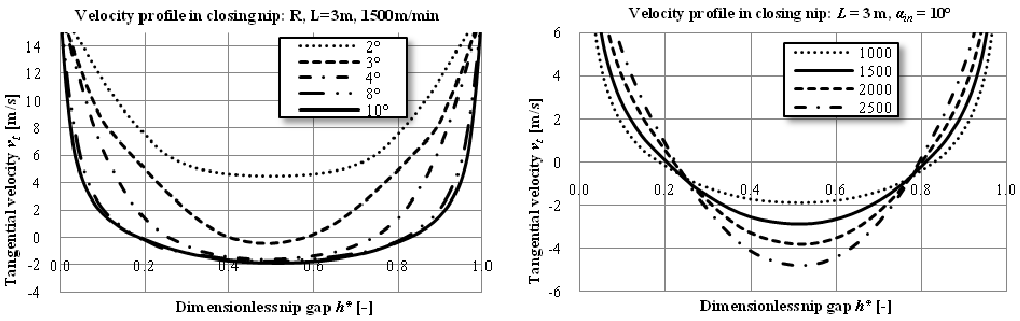

Figure 12: *a)* Velocity profiles from the closing nip angles 2°-10°, *b)* Variation of surface velocities.

Changes in the boundary layer development lengths L can be seen to affect the velocity profiles when $\alpha_{in} > 10°$, which is caused by the stronger boundary layer flows. When $\alpha_{in} < 10°$, the backflow breaks the boundary layer flows. In Figure 13*a*, the curves at $\alpha_{in} = 10°$ are taken from models where L is varied between 1 to 3 m, namely L1, L2 and L3. The velocity profile curves are almost identical.

According to the simulation models, the closing nip pressures are identical when the boundary layer development length is changed. In this light, Karlsson's theory [18], which predicts pressure changes in the closing nip when L is changed, should be questioned. The CFD model simulation results show that the backflow coming from the closing nip disturbs the boundary layer flows, and the static pressure increases only two Pascals in the closing nip. In Figure 13*b*, the static pressure curves are shown as a function of the nip angle. The L1 curve is the continuous black line, L2 is marked with the plus sign, and L3 with the x-sign.

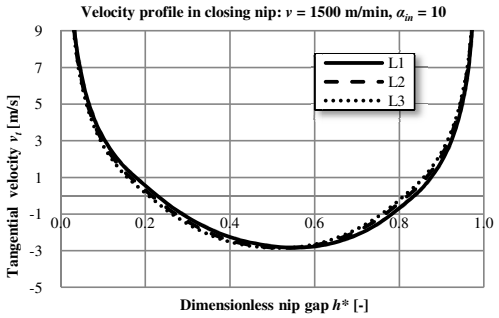

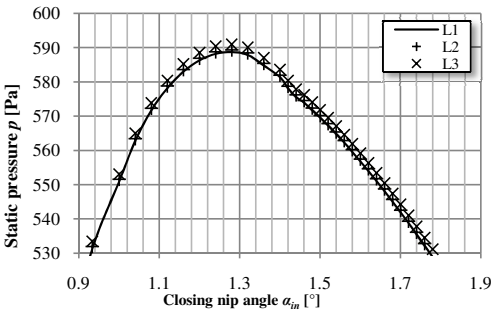

Figure 13: *a)* Velocity profile at α_{in} = 10°, varying L from 1 to 3m, *b)* Static pressure on wall surface with variation of L from 1 to 3m.

With larger nip angles α_{in} 20° and 30°, shown in Figures 14*a* and *b*, changes in the boundary layer thickness can be seen. Close to the horizontal wall, the tangential velocity is larger when L = 3 m, which is in agreement with boundary layer theories, according to which the velocity profile is distorted closer to the wall (when L = 1 m).

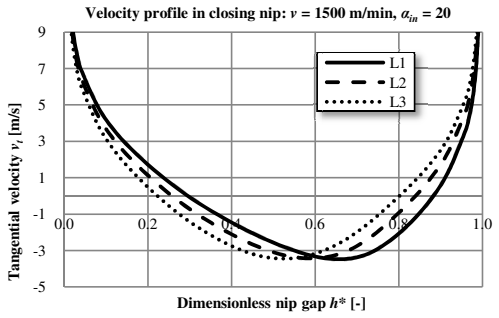

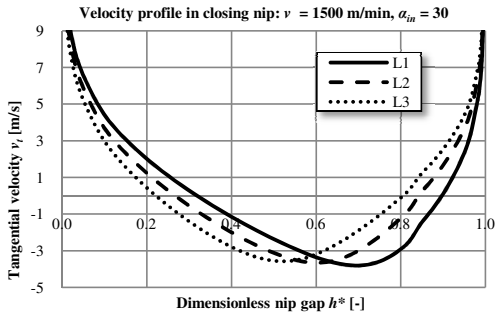

Figure 14: *a)* Velocity profile at α_{in} = 20°, varying L from 1 to 3m, *b)* Velocity profile at α_{in} = 30°, varying L from 1 to 3m.

Evaluation of the turbulence in the closing nip is a challenge. The Reynolds number in the closing nip explained in Section 2.1.1 is calculated with Equation 3. In Figure 15, the

Reynolds number Re is presented as a function of the closing nip angle α_{in}. The surface velocities are varied from 1000 m/min to 2500 m/min. The computational geometry is as follows: L is 3 m and the roll radius r is R. The surface velocities affect the points when the flow changes from turbulent to laminar. With the lowest velocity, transition to laminar is at 11.4°, and with the highest velocity it is 6.8°. The turbulence transition zone ($2300 < Re < 4200$) is wider with the lowest velocity. In the curve of 1500 m/min, an exception can be seen at Re = 4200. A closer examination of the result shows small differences in flow structures (swirl) compared to the other curves.

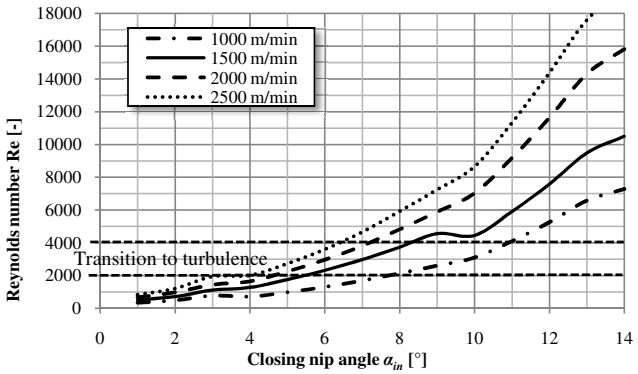

Figure 15: Closing nip turbulence varying the surface velocity.

Figure 16 presents the velocity vectors from the closing nip, colored by the velocity magnitude. The velocity profiles at 10°, 20° and 30° are shown with dotted lines. The boundary layer flows more along the surfaces and mixes at the closing nip. The origin of the backflow is shown. The velocity vectors clearly show backflow in the middle of the nip, where it flows from right to left.

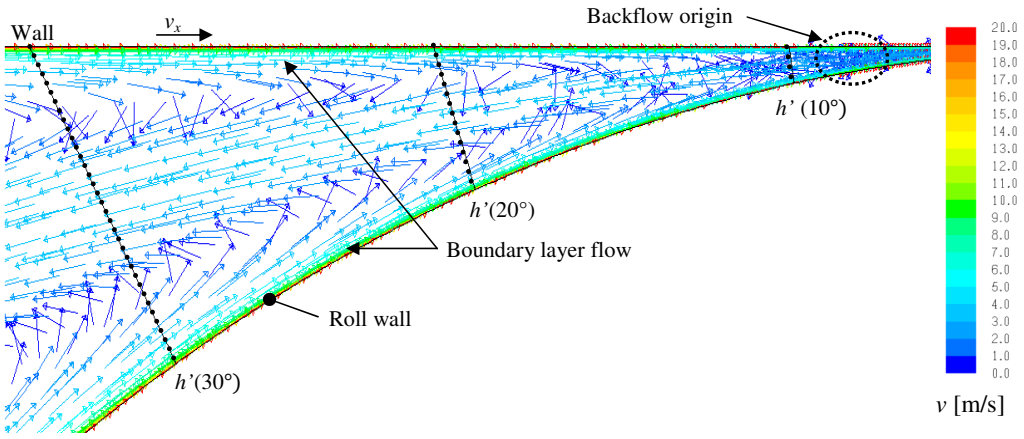

Figure 16: Air flow at the closing nip presented with velocity vectors.

2.1.3 Opening nip

Kurki has derived the analytical opening nip pressure assuming that the air flow is a laminar Couette flow with a parabolic velocity profile without air leakage to the nip. The opening nip pressure is given by Equation (5) [21].

$$p(x) = \frac{8a\rho_a\mu_a v_x r^2}{3x^3}, x > 0, \tag{5}$$

where a is an empirical coefficient 6, μ_a is air viscosity, and x is the distance from the nip. Note that for $p(x) \to \infty$ as $x \to 0$, which is unrealistic.

At the opening nip, the boundary layers start to grow, and the changes in the boundary layer development length on the closing nip side do not affect the opening nip side flows. The velocity profiles are used to describe the flow, similar to the closing nip. A negative tangential velocity indicates inflow directed towards the opening nip. As a comparison, the maximum value of the inflow at opening nip with 10° angle is -2.0 m/s, whereas in the closing nip side it is -2.8 m/s. In Figure 17*a*, the opening nip velocity profiles are shown with different opening nip angles. The used CFD model geometry was described in Section 2.1.1. The curve shapes are slightly flat-headed, compared to the closing nip curves. Widlund [51] has measured the opening nip velocity profile with the smooth roll and permeable fabric showing similar velocity profiles. The effect of surface velocity changes can be seen in Figure 17*b*. When the velocity is increased, the inflow increases as well.

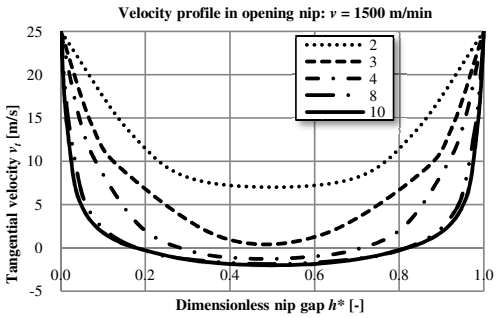

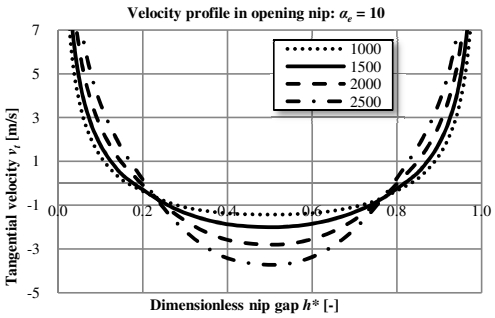

Figure 17: *a)* Air Velocity profiles from the opening nip angles 2°-10°, *b)* Variation of surface velocities.

A comparison of the opening and closing nip Reynolds numbers as a function of nip angle shows differences when the angles are larger than 8°, see Figure 18. The closing nip Reynolds number is larger when $\alpha > 11.4°$ compared to the opening nip. This is due to stronger boundary layer flows at the closing nip surfaces. In the closing nip curve, an exception can be seen at $9 < \alpha > 10.5°$. A closer examination of the result shows small differences in the flow structures.

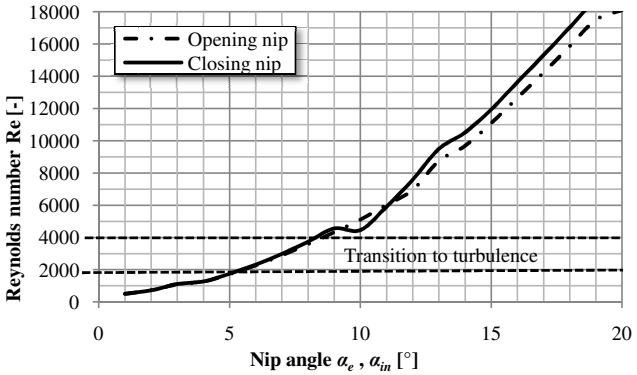

Figure 18: Comparison of the closing and opening nip turbulence with velocity of 1500 m/min.

In Figure 19, the velocity vectors illustrate opening nip boundary layer flows starting to develop from the nip. Inflow can be seen between the developing boundary layers, filling the opening nip underpressure area near the roll and horizontal wall tangent point.

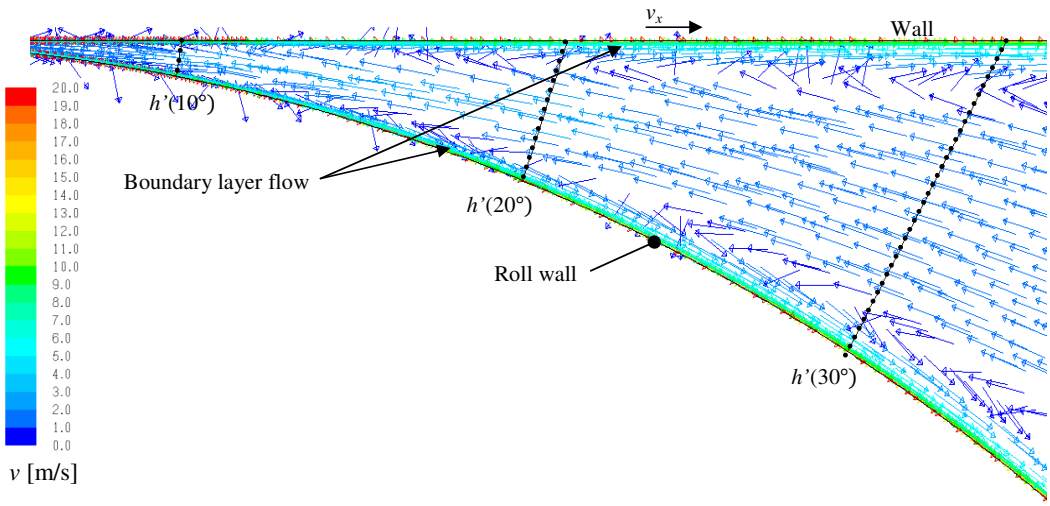

Figure 19: Air flow at the opening nip presented with velocity vectors.

2.1.4 Static pressure at the closing and opening nips

Pressure curves calculated with the 2D smooth roll CFD model with small wrap angle are presented and compared to theoretical ones. In the CFD model, the variables are velocity and roll radii. The theoretical pressure curves have been obtained by using Equation (4) for the closing nip, and Equation (5) for the opening nip. Figure 20 and Figure 21 are the first results published by the author of this thesis [38] where the closing and the opening nip solutions are coupled.

The closing nip x-coordinates are $-0.15 < x < 0$ m, and those of the opening nip $0 < x < 0.15$m. The flow development length L is 3 m, and the surface velocity 2000 m/min. The air density ρ_a is 1.17 kg/m³ and viscosity μ_a is 1.5 x 10^{-5} kg/ms. The roll diameters represent typical roll sizes in a paper machine. The pressure curves have been taken from the horizontal wall surface, where the tangent point is located at $x = 0$.

With a small roll radius, the area of the affecting pressure is smaller than for a large roll radius. In the case of a large roll, the nip areas are longer. In the closing nip region, the theory overestimates the maximum pressure, and in the opening nip region the maximum underpressure. In the smooth roll, the air entrainment height $L_{e,h}$ of the CFD model is constant 100 µm. The connection between the closing and opening nip is obvious; the pressure starts to decrease before the tangent point. Figure 20 shows static pressure as a function of the x-coordinate.

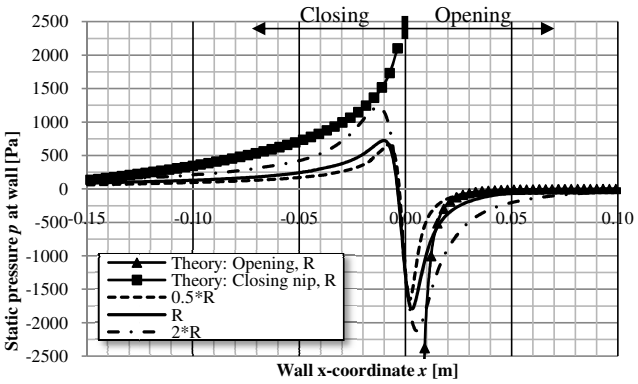

Figure 20: Pressure distribution in the closing and opening nip with different roll radii.

The variations of the wall and the roll surface velocity clearly show the pressure behavior: in the closing nip region, the maximum pressure and affecting area increase when the surface velocity is increased, and the maximum and minimum nip pressures are achieved at smaller x values with higher velocities. Figure 21 presents the closing and opening nip pressure as a function of the wall x-coordinate.

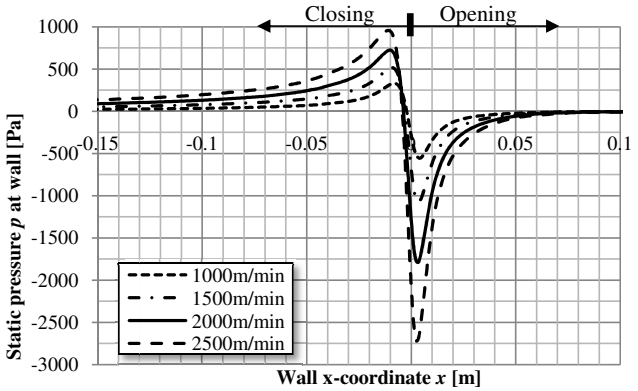

Figure 21: Effect of surface velocity on the pressure distribution with the roll radius R.

The boundary layer flows are unavoidable near the moving surfaces. The overpressure in the closing nip affects the runnability, which can be seen in the real web handling device as increased air entrainment and web deformations. One possibility to avoid overpressure in the closing nip is to guide the boundary layer flow away from the closing nip or through the nip by using a grooved roll.

2.2 *3D grooved roll*

A micro-grooved roll has been proven to lower the air entrainment [6] and improve the traction [9]. When the surface velocities are high, the boundary layer flows increase. The groove size is an important factor when considering air entrainment and closing nip overpressure, which are not desired features. A grooved roll surface offers a route for the boundary layer flow to escape from the narrowing nip area; and therefore the closing nip overpressure reduces. The grooved roll has been noticed to create underpressure to grooves covered with fabric or paper web [22]. The boundary layer flow experiences minor and viscous flow losses when traveling through the nips and groove. In the following, the aerodynamic functionality of the grooved roll is introduced.

The grooved roll CFD model-geometry is a three-dimensional "*slice*", which consists of a wall on top, a half groove and a half of a roll land with symmetric (reflection) boundary conditions. This simplification reduces the computational effort without compromising accuracy. The CFD model describes the roll and wall as infinitely wide, capturing entrance, exit, and friction effects between the groove and the surrounding air. The moving wall tension is assumed to be infinite, referring to discussion related to fluid structure interaction simulation in Section 1.4. The grooved roll configuration with nomenclature is presented in Figure 22. $L_{g,h}$ is groove height, $L_{g,w}$ is groove width, $L_{l,w}$ is roll land width and $L_{e,h}$ is the gap between the roll land and the wall.

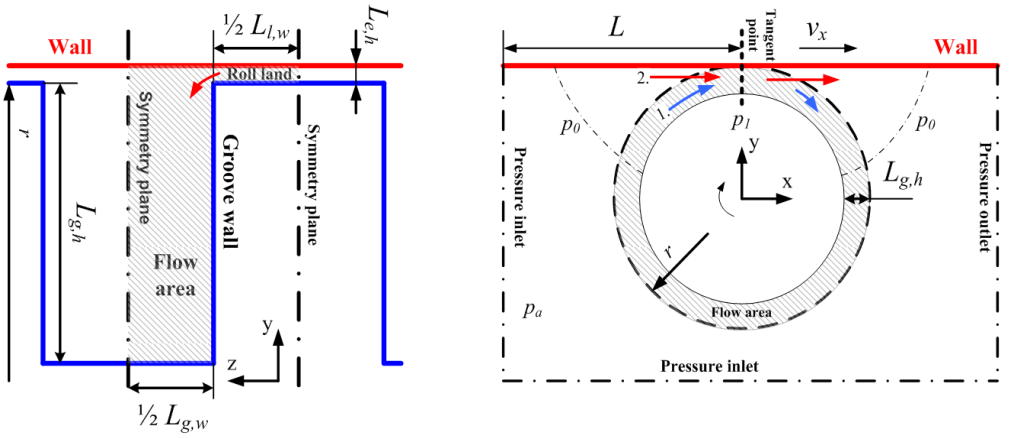

Figure 22: 3-dimensional model for a grooved roll and the associated nomenclature and boundary conditions.

Air has two primary routes to reach the tangent point of the roll and wall: the first one (arrow 1 in Figures 22 and 23) is from within the roll groove. The second one (arrow 2 in Figures 22 and 23) is the flow along the wall to the closing nip, where the flow bends to the groove. Depending on the wall velocities, the development length of the boundary layer and the groove geometry, the air flow accelerates to a high speed at the tangent point. The air acceleration causes underpressure in the groove due to an increase of dynamic pressure. A challenge now arises: what are the flow losses in route 2? The flow experiences so called minor losses in the sudden contraction and change of flow direction. At the same time, the friction losses in the groove and the converging area between the wall and the groove land increase the flow losses. The assumption of frictionless flow cannot be made, and therefore the simple Bernoulli equation approach of Kurki [22] cannot explain these losses. In Figure 23, a groove function principle and the causes of pressure losses is presented. Static pressure p_1 is determined on the basis of the pressure losses in the nips and in the groove, as well as the driving forces coming from the boundary layer flows.

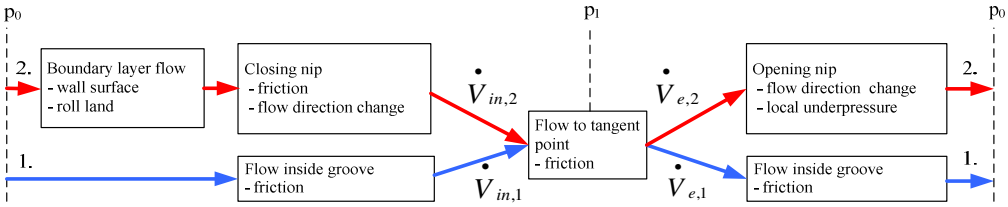

Figure 23: Operating principle of the 3D grooved roll model with nomenclature.

Subscript *in* stands for the closing nip flow, and *e* for the opening nip flow. Subscript 1 stands for the flow in the groove, and 2 for boundary layer flow along the wall surface. Since the flow solutions are strongly coupled, the volume flows are the same at the closing and opening nip. According to the roll size, the groove geometry and boundary layer flows, the volume flow proportions change. On the closing nip side, the groove filling fraction V_f is defined as

$$V_f = \frac{\dot{V}_{in,2}}{\dot{V}_{in,1} + \dot{V}_{in,2}} \tag{6}$$

where $\dot{V}$ is the volume flow. Similarly, the groove emptying fraction V_e is

$$V_e = \frac{\dot{V}_{e,2}}{\dot{V}_{e,1} + \dot{V}_{e,2}} \tag{7}$$

The flow characteristic Reynolds number in the groove is defined as

$$\mathrm{Re} = \frac{\rho_a v_{rel} d_h}{\mu_a}, \text{ where the hydraulic diameter } d_h = \frac{4(L_{g,w} \cdot L_{g,h})}{2(L_{g,w} + L_{g,h})}. \tag{8}$$

The relative velocity for air is defined as $v_{rel} = v_a - v_x$, where v_a is the air velocity in the groove, and v_x is the wall velocity. The filling fraction V_f and emptying fraction V_e, as well as the Reynolds number Re and hydraulic diameter d_h are used later in this thesis to evaluate the 3D and 2D CFD simulation results.

2.2.1 Flow losses due to entrance and exit

The aerodynamic properties of the grooved roll at the closing and opening nips depend among other things, on the groove geometry, roll radius and surface velocity. The air flow path number 2 in Figure 23 depends on the minor losses. At the air flow entrance and exit, so called minor losses can be obtained from the 3D grooved roll CFD model.

The defined grooved roll parameters are the groove filling angle α_f at the filling point, the area weighted average pressure at wall $\overline{p}_{wall}$ (double dash dotted line) and near the groove top $\overline{p}_g$ (dash dotted line), shown in Figure 24. The groove filling angle α_f is measured from the 3D grooved roll CFD model from the groove top at radius r, where radial velocity v_{rad} is negative on the closing nip side, and on the opening nip side v_{rad} is positive. The groove filling angle is counterclockwise positive, starting from the tangent point. The opening nip side pressures are defined in a similar manner. The subscript for the closing nip side filling is *f,* and for the opening nip side emptying, the subscript is *e*.

The area for the affecting pressure is obtained on the basis of the filling angle at the groove top and wall surface. The curve length of the groove top affecting pressure area, denoted with $\overline{p}_g$, is used at the wall surface as the length of $\overline{p}_{wall}$. The average radial filling velocity $\overline{v}_{rad}$ and average wall radial velocity component $\overline{v}_1$ are measured from the 3D grooved roll CFD model.

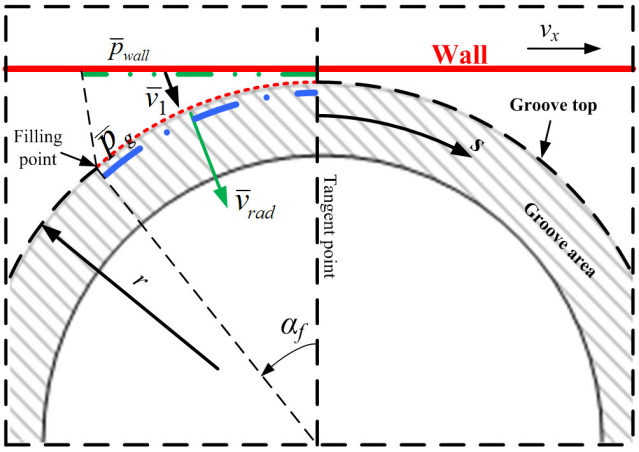

Figure 24: The groove filling area with nomenclature.

As the flow experiences friction and minor losses, the simple Bernoulli equation approach of Kurki [22] cannot explain these losses. Adding the minor loss term with the minor loss coefficient K to the Bernoulli equation yields

$$\overline{p}_{wall} + \frac{1}{2}\rho_a(\overline{v}_1)^2 + \rho_a g y_1 = \overline{p}_g + \frac{1}{2}\rho_a(\overline{v}_{rad})^2 - K\frac{1}{2}\rho_a(\overline{v}_{rad})^2 + \rho_a g y_2\,, \tag{9}$$

where $y_1 = y_2$. The minor loss coefficient K can be solved from Equation (9)

$$K = 1 - \frac{\frac{2(\overline{p}_{wall} - \overline{p}_g)}{\rho_a} + \overline{v}_1^2}{\overline{v}_{rad}^2} \tag{10}$$

The minor losses depend on the boundary layer flow and the groove size. In Figure 25, flow path lines are shown with a narrow and wide roll land. The used geometry is presented in Figure 22. With the wide roll land, the boundary layer flow has to change its direction more than with the narrow roll land.

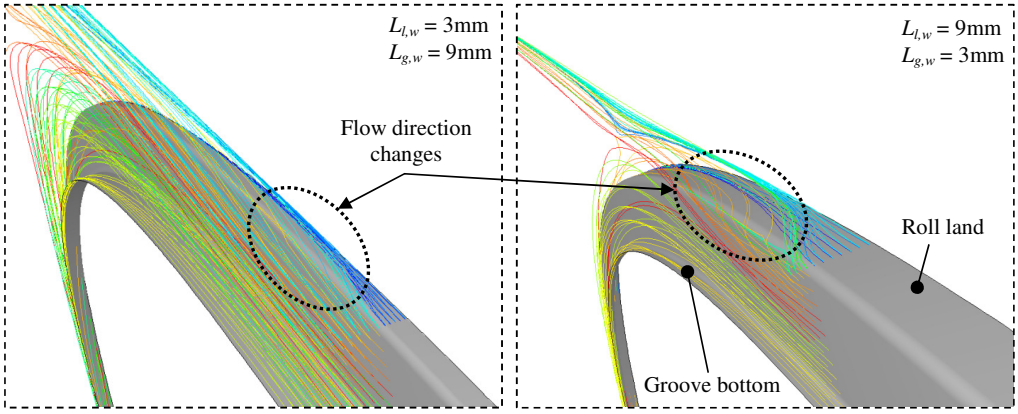

Figure 25: The effect of the roll land on the flow path lines, *a)* a narrow roll land, *b)* a wide roll land.

Air entrainment to the small gap between the web and the roll land generates an extra loss, which is difficult to define analytically because of the complex flow area. This phenomenon is similar to the case of the smooth roll opening and closing nip pressures. The 3D grooved roll CFD model captures the boundary layer flow losses through the grooved roll nips and the groove.

2.2.2 Flow friction losses in the groove

The groove wall friction effects are calculated analytically with the equations of viscous fluid flow in ducts. This approach of calculating the flow friction losses in grooves is used in Section 2.3. The duct is assumed to be infinitely long and straight, with hydraulically smooth surfaces. The pressure gradient is

$$\frac{dp}{ds} = \frac{f}{d_h}\frac{\rho_a v_{rel}^2}{2}, \tag{11}$$

where s is the groove tangential coordinate, f is the friction coefficient and d_h is defined as in Equation (8). The friction coefficient depends on the Reynolds number, and it is shown in Equation (12) [50].

$$\begin{cases} f_{lam} = \dfrac{64}{\mathrm{Re}} & \mathrm{Re} < 2300 \\ f_{turb} = 0.316\,\mathrm{Re}^{-1/4} & 4000 < \mathrm{Re} < 10^5 \end{cases} \tag{12}$$

2.2.3 Simulation results of the 3D grooved roll

The following results are based on the 3D grooved roll CFD simulations described above. The pressure curves have been plotted from the horizontal wall surface as a mean value to the *z*-coordinate. In other words, at tangent point, the effect of the roll land and the groove can be seen. The tangent point of the model is at location x = 0. The flow development length (L = 3 m) is constant in the next simulation results. In the following, changes in surface velocities, groove width and groove height, as well as the roll radius are presented. The 3D grooved roll CFD model with nomenclature is shown in Figure 22.

In Figure 26, the surface velocities are changed. Static pressure is plotted as a function of the *x*-coordinate. The roll radius is R. The maximum pressure on the closing nip side is around 100 Pa for 2500 m/min. The minimum pressure is just after the tangent point, at the opening nip side. The variations in the pressure curves at -0.02 < x < 0.0 m are related to friction and minor losses where the wall is very close to the roll land. At x < -0.10 there is some development of overpressure to the closing nip side, which is not desirable for paper machine environments. Static pressure decreases at the tangent point when the dynamic pressure increases. The air flow is turbulent at the tangent point inside the groove. The Reynolds number Re varies between (1000 - 2500 m/min) 5000 and 11700. The static pressure at the tangent point clearly decreases with increased velocity. The positive pressure in the closing nip increases when the velocity is increased.

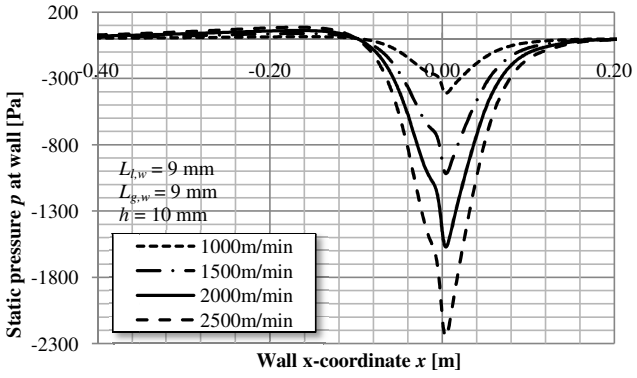

Figure 26: Effect of velocity v_x on the pressure distribution.

Groove height adjustment increases the cross-sectional flow area in the grooves. This helps the boundary layer flows to fit into the grooves with lower pressure in the closing nip

area. A roll with deeper grooves has now a higher ability to move the air between the closing and opening nip. The maximum underpressure at the tangent point is the same with groove heights 10 mm and 20 mm, but with groove height 5 mm, the underpressure is reduced. In Figure 27*a*, the pressure distribution for three groove heights and a smooth roll is presented. Comparison with the smooth roll reveals a significant difference in the pressure development. The groove reduces the closing nip pressure closer to the ambient pressure.

The roll radius influences the pressure distribution. A larger roll radius results in a wider underpressure area. From the web handling point of view, a wide underpressure area could be desirable. The maximum underpressure is the lowest with the smallest roll radius, but at the same level for the two larger rolls. Figure 27*b* shows the effect of roll radius on the pressure distribution.

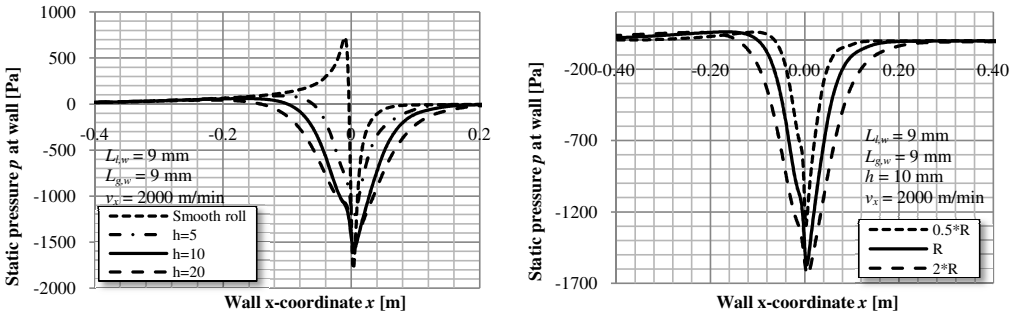

Figure 27: *a)* Effect of groove height on the pressure distribution, *b)* Effect of roll radius on the pressure distribution.

Variations of groove width $L_{g,w}$ and roll land $L_{l,w}$ when the groove height $L_{g,h}$ and surface velocity are kept constant give more information about the pressure distribution at the wall surface in the vicinity of the closing and opening nips. Based on the groove and the roll land width, the dimensionless measure groove fraction G_f is defined as in Equation (13)

$$G_f = \frac{\text{Groove area}}{\text{Groove area} + \text{Roll land area}} = \frac{L_{g,w}}{L_{g,w} + L_{l,w}} \tag{13}$$

A wide groove compared to the roll land width gives beneficial results for the pressure distribution. The closing nip overpressure is lower without losing much of the underpressure at the tangent point. When the roll land is wide, the friction and minor losses at the nip areas increase, which affects the underpressure distribution. In Figures 28*a* and *b*, the groove width and roll land measures are modified.

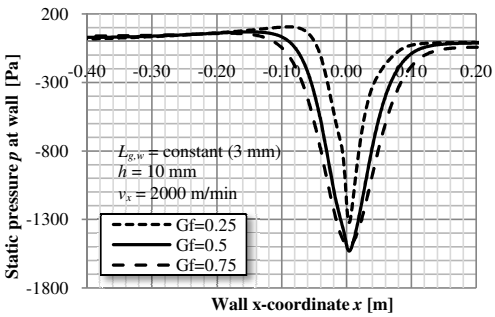

Figure 28: *a)* Effect of roll land on the pressure distribution,

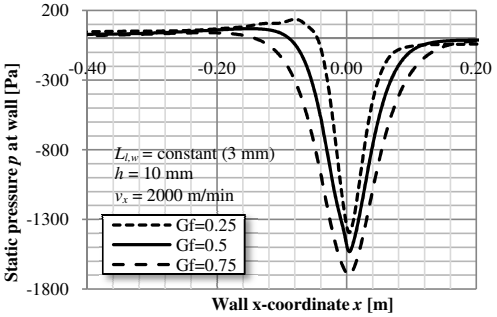

b) Effect of groove width on the pressure distribution.

2.3 *2D grooved roll simulation tool*

The purpose for the grooved roll CFD simulation tool is to simulate 3D grooved roll effects with a 2-dimensional model. In the 2D model, the groove height, width, friction and minor losses are modeled with porous media and porous jump boundary conditions. This is called the 2D grooved roll simulation tool (GRT). The 2D grooved roll model with the boundary conditions is shown in Figure 29.

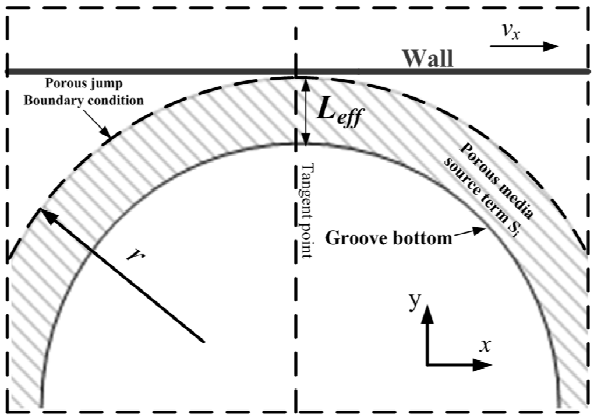

Figure 29: 2D grooved roll model with boundary conditions and nomenclature.

The groove cross-sectional area is converted to the 2D model with effective groove height L_{eff}. Rice [43] has used a similar method for effective groove height. This way the groove cross-sectional area and volume flow through the groove is the same with both the 3D grooved roll model and the 2D grooved roll model. For a rectangular shaped groove, the effective groove height L_{eff} is

$$L_{eff} = \frac{L_{g,w} \cdot L_{g,h}}{L_{g,w} + L_{l,w}} \tag{14}$$

In Figure 30, the modification from the 3D groove to 2D effective groove height is presented from the cross direction point of view.

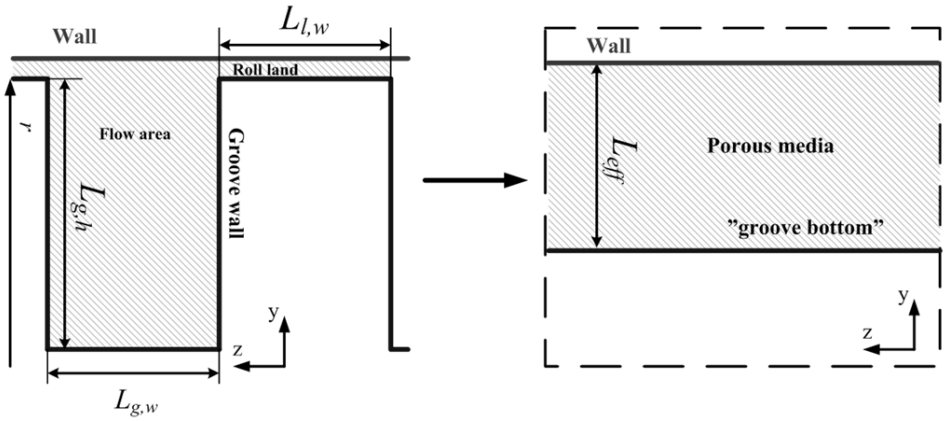

Figure 30: Effective groove height modification with nomenclature.

The groove wall friction effects are calculated with the equations of viscous fluid flow in ducts. The surfaces are assumed to be hydraulically smooth. The grooved area friction source term S_s is obtained with a second degree polynomial curve fit by combining Equations (11) and (12). The air velocity v_s is chosen in the range 0 to 30 m/s. The source term S_s is

$$S_s = -(Dv_s + Cv_s^2), \tag{15}$$

where D is the viscous loss term and C is the inertia loss term [8]. The minor pressure loss explained in Section 2.2.1 is modeled in 2D by using the porous jump boundary condition in the outer surface of the grooved roll. The minor pressure loss expressed with the porous jump boundary condition is

$$\Delta p = -\left(\frac{\mu_a}{\alpha} v_{rad} + C_{2D} \frac{1}{2} \rho_a v_{rad}^2\right) \Delta m, \tag{16}$$

where α is the permeability of the medium, C_{2D} the porous-jump coefficient, and Δm is the thickness of the medium [8]. The 2D model is not able to capture the flow area change in the axial direction of the roll, and therefore the minor loss coefficient K calculated with the help

of the 3D grooved roll model has to be modified. Based on the continuity, the porous jump coefficient C_{2D} is

$$C_{2D} = \frac{K}{G_f^2} \tag{17}$$

In practice, the porous jump coefficient C_{2D} is obtained experimentally. The volume flow of the 2D grooved roll model has to be equal to the corresponding 3D grooved roll model volume flow. A solution strategy for 2D grooved roll simulations is presented in Section 2.3.2.

2.3.1 Simulation results of the 2D grooved roll model

In the following, CFD simulation results of a 3D and 2D grooved roll interacting with a moving horizontal wall are presented. In both CFD models, air is treated as ideal gas. The system is assumed adiabatic, where the temperature is T = 300K. The roll and wall surfaces are assumed to be hydraulically smooth. The volume flow through the 2D grooves are adjusted with the porous jump boundary condition (see Equation 16) to be the same as with the 3D grooved roll model.

The pressure curves from the 3D grooved roll CFD model have been plotted from the horizontal wall surface as an area-weighted mean value to the z-coordinate. In other words, the effect of the roll land and the groove can be seen at the tangent point. The tangent point of the model is in location x = 0 or α = 0. The closing nip is located at x < 0, and the opening nip at x > 0. The flow development length (L = 3m) is constant in the 2D and 3D grooved roll models. In the following, changes in surface velocities, groove width and groove height, and the roll radius are presented.

The filling of the groove is measured from the top of the groove. The groove filling point is where $v_{rad,f} = 0$ and the filling angle is α_f. Similarly, the emptying point is at $v_{rad,e} = 0$, and the emptying angle is α_e. In order to compare the radial velocities between the 2D and 3D grooved roll CFD models, the 2D radial velocity needs to be modified as shown in Equation (18).

$$v_{rad}^{*} = \frac{v_{rad,2D}}{G_f} \tag{18}$$

In Figure 31, the radial velocity at the groove top is presented with nomenclature as a function of the roll angle α. A comparison of the radial velocity curves in 2D and 3D grooved roll CFD models is shown as an example. The 3D grooved roll CFD model is marked with a continuous line and the 2D grooved roll CFD model with a dash-dotted line. The used geometry is the reference point, where the roll radius is R. As a result, the 2D CFD model seems to give almost the same radial velocity curve as the 3D model. The maximum radial velocity on both nips can be found approximately at the angle of 5°.

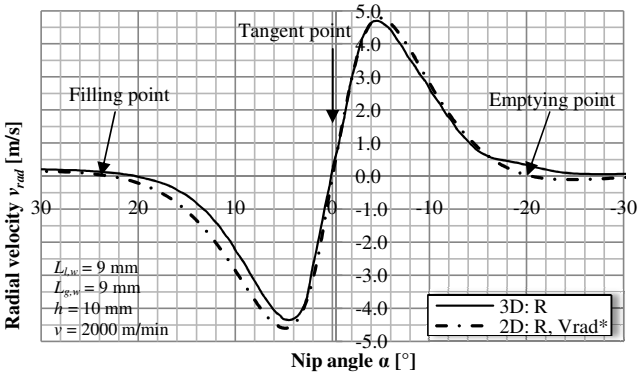

Figure 31: Radial velocity at the closing and opening nips with the 2D and 3D CFD models.

For each model, some characteristic values can be used to evaluate the groove performance and functionality. In table 1, filling fraction V_f and angle α_f, as well as the groove minor loss K for the 2D and 3D models are shown. The rows present changes to the roll geometries in order to see the changes in the roll performance. The first row is the reference geometry. The roll properties which are changed are shown in the first column as underlined and bolded values.

A comparison of the 2D and 3D CFD models reveals that the filling angle behaves rather linearly, overestimating systematically 3 degrees with the 2D model. The filling fraction and minor losses show that the friction in the very narrow closing nip area between the roll land and wall has a greater effect than assumed by the author of this thesis. When the roll radius is doubled, the 2D CFD model needs a significantly greater minor loss coefficient in order to maintain the desired volume flow through the groove. It needs to be reminded that the used source term S_s is based on an assumption of groove friction shown in Equations (11-12), which affects the flow parameters as well.

Table 1: Aerodynamic properties of selected 2D and 3D grooved roll models.

r-$L_{g,w}$-$L_{l,w}$-$L_{g,h}$-v	$V_{f,3D}$ [-]	$V_{f,2D}$ [-]	$\alpha_{f,3D}$ [°]	$\alpha_{f,2D}$ [°]	K [-]	$C_{2D,exp}$ [-]
R-9-9-10-2000	0.460	0.694	20.4	23.1	11.3	24.4
R-9-9-10-**1000**	0.625	0.692	18.9	22.3	11.7	25.3
R -9-9-**20**-2000	0.563	0.685	26.7	32.4	15.0	8.8
2R-9-9-10-2000	0.308	0.705	13.8	17.0	5.5	43.5
R -**3**-9-10-2000	0.474	0.591	11.4	14.5	9.7	12.7
R -9-**3**-10-2000	0.639	0.707	25.2	29.2	21.7	4.2

In Figure 32, the surface velocities are varied. Static pressure is plotted as a function of the x-coordinate. The roll radius is R. Static pressure decreases at the tangent point when the dynamic pressure increases. The air flow is turbulent at the tangent point in the groove. The Reynolds number Re varies between (1000 - 2000 m/min) 5000 => 11700.

A comparison between the 2D and 3D CFD models reveals that at the closing nip side x < -0.02 and opening nip side x > 0.02m, the pressure curves are identical. The maximum pressure on the closing nip side is around 50 Pa for 2000 m/min for 2D and 3D CFD models, which is not desirable for paper machine environments. The minimum pressure is just after the tangent point, at the opening nip side with the 3D CFD model. The highest underpressure locates at the tangent point with the 2D CFD model. Variations in the pressure curves at -0.02 < x < 0.02 m are related to the friction and minor losses with the 3D CFD model, where the wall is very close to the roll land. At the tangent point, the 2D grooved roll CFD model underestimates the underpressure. The 2D grooved roll CFD model uses the averaged approach because of the porous media boundary conditions, and therefore small variations in the curves cannot be seen.

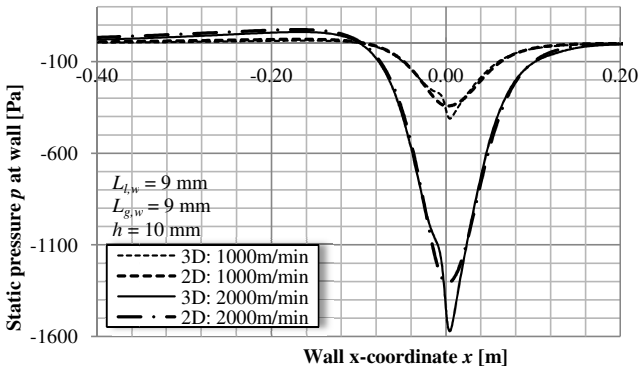

Figure 32: Effect of velocity v_x on pressure distribution with the 2D and 3D models.

Groove height adjustment increases the cross-sectional flow area in the grooves. This helps the boundary layer flows to fit into the grooves with lower pressure in the closing nip area. A roll with deeper grooves has now higher ability to move the air between the closing and opening nip. The 2D and 3D CFD models are in a good agreement, and differ only slightly from the closing and opening nip sides. In Figure 33, the pressure distribution for the groove height of 20mm is presented with the 2D and 3D CFD models.

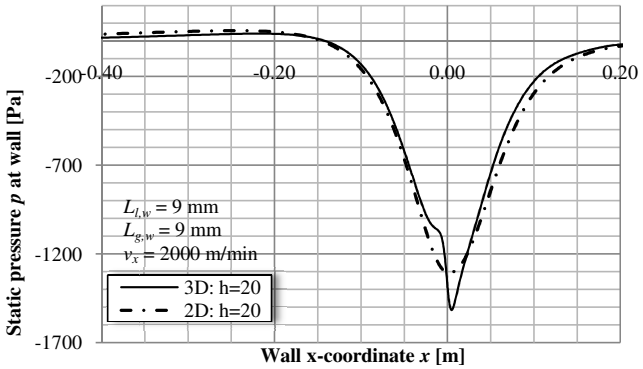

Figure 33: Effect of groove height on the pressure distribution; a comparison between the 2D and 3D CFD models.

The roll radius influences the pressure distribution. A larger roll radius results in a wider underpressure area. From the web handling point of view, a wide underpressure area could be desirable. The 2D CFD model overestimates the closing nip overpressure by about 50 Pa. At the tangent point, the 3D CFD model predicts a slightly higher underpressure. Figure 34 shows the pressure distribution with roll radius 2*R*. The 2D and 3D models are compared.

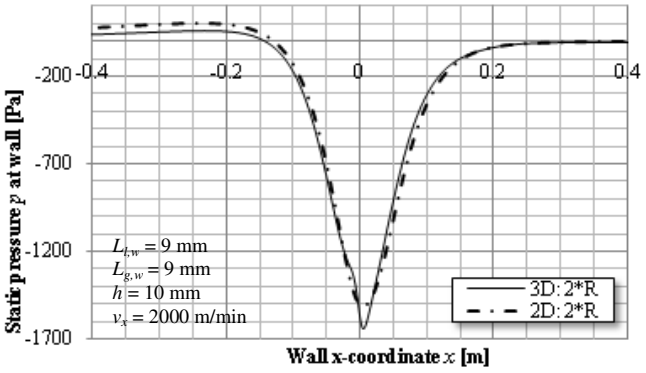

Figure 34: Effect of roll radius on the pressure distribution with the 2D and 3D models.

Variations of the groove width $L_{g,w}$ and roll land $L_{l,w}$, when the groove height $L_{g,h}$ and surface velocity are kept constant gives more information about the pressure distribution at the wall surface in the vicinity of the closing and opening nips.

A wide groove compared to the roll land width gives beneficial results for the pressure distribution. The closing nip overpressure is lower, without losing much of the underpressure at the tangent point. When the roll land is wide, the friction and minor losses at the nip areas increase, which affects the underpressure distribution. The narrower groove with the 2D CFD model gives a better estimation on the location of the highest under pressure peak. When the groove land is narrow compared to the groove width, the 2D CFD model gives a very accurate prediction for the pressure at the wall surface. Only small overestimation in the closing nip pressure can be observed. In Figures 35*a* and *b*, the groove width and roll land measures are modified, and the results are compared between the 2D and 3D CFD models.

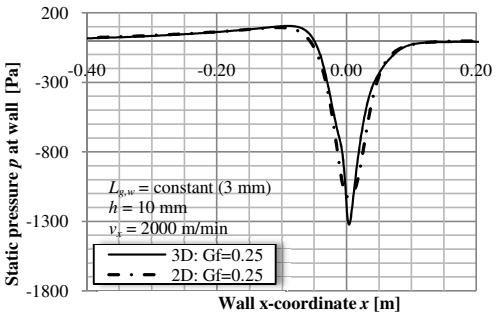

Figure 35: *a)* Variation of roll land with the 2D and 3D CFD models,

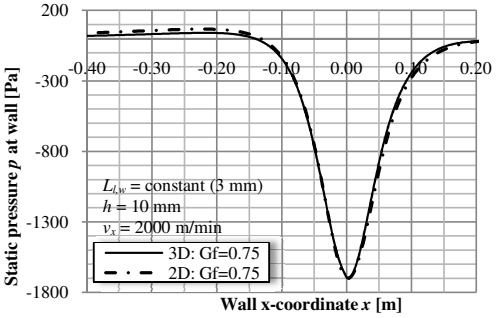

b) Variation of groove width with the 2D and 3D CFD models.

2.3.2 Solution strategy for 2D grooved roll simulations

Before the simplified 2D grooved roll model can be used in full scale paper machine environment simulations, the following procedure needs to be performed as a solution strategy for the grooved roll simulations. In the first step, a simple 3D model is created, based on the grooved roll geometry where the groove dimensions and roll size, as well as the machine speeds are known. The simple 3D CFD model consists of a moving wall and a grooved roll (See Figure 22 for details). In the model, a symmetric slice of a half groove and half roll land is modeled. As a result, the volume flow through the groove and the static pressure in the groove are obtained.

In the second step, a 2D grooved roll CFD model is created. The model simplifications with effective groove height L_{eff}, source term describing friction S_s and initial guess of porous-jump coefficient C_{2D} are made. The porous-jump coefficient is adjusted until the volume flow $\dot{V}_{2D}$ through the groove is equal to $\dot{V}_{3D}$. When the fine tuning of the 2D grooved roll CFD model is done, it is ready to be used in complex paper machines or web handling applications to evaluate the grooved roll functionality in the chosen environment. A solution strategy for the grooved roll models is shown schematically in Figure 36.

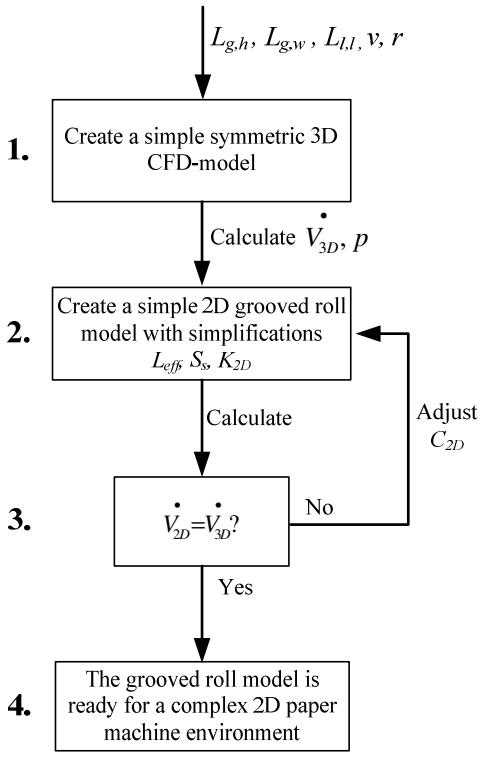

Figure 36: A solution strategy for the grooved roll model.

2.3.3 Fabric model

In the paper machine environment, the rolls interact with permeable walls, namely drying fabrics in the tail threading phase. The fabrics support and transport the paper web through the paper machine. It is important to know how the fabrics affect the aerodynamic functionality of the grooved roll. The fabric has several aerodynamic features affecting the boundary layer

flows, such as air permeability, void volume, structure and yarn type [7]. Two dryer fabric structures are introduced: woven fabric (Figure 37 *a*) and a spiral fabric structure (Figure 37 *b*).

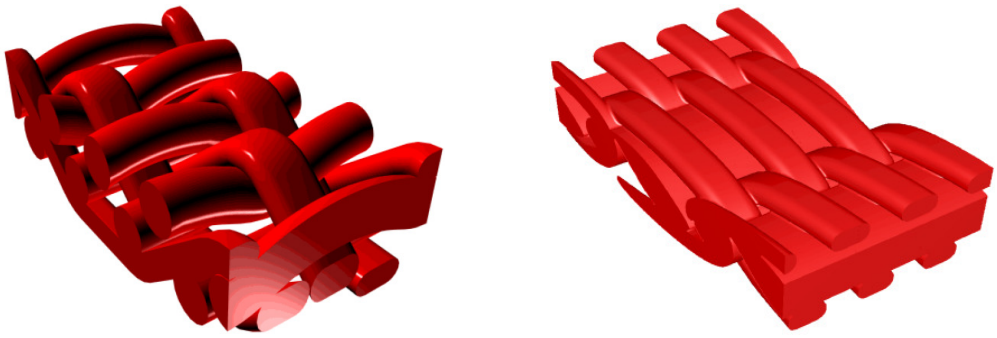

Figure 37: *a)* Woven drying fabric [27], *b)* Spiral drying fabric [27].

In this thesis, the grooved roll interacting with the fabric is studied by using CFD models. In the previous sections only smooth surfaces were considered as momentum sources of boundary layer flows. The fabric surface is rough, typically between 0.2 to 0.5mm [19]. The ability of the surface roughness and fabrics to carry air increases the pressure in the closing nip areas [19]. The fabric structure allows the air to flow through the fabric, if the pressure difference over the fabric surfaces is sufficient. Air flow through the fabric from the closing nip side can cause detachment of the paper web from the fabric surface [25]. In the case of a grooved roll partly covered with drying fabric, it is important to see the air flow behavior in the nip areas and to find out whether there is underpressure in the grooves.

The fabric model applied in this study has been introduced by Laakkonen [25]. The detailed fabric functionality is not discussed in this work. The fabric model describes the aerodynamic properties of fabric in large scale with the help of a porous media simulation model in Cartesian coordinates shown in Equation (19) [25]

$$\begin{pmatrix} f_x \\ f_y \\ f_z \end{pmatrix} = \begin{pmatrix} D_{11} & D_{12} & D_{13} \\ D_{21} & D_{22} & D_{23} \\ D_{31} & D_{32} & D_{33} \end{pmatrix} \begin{pmatrix} U \\ V \\ W \end{pmatrix} + \begin{pmatrix} C_{11} & C_{12} & C_{13} \\ C_{21} & C_{22} & C_{23} \\ C_{31} & C_{32} & C_{33} \end{pmatrix} \begin{pmatrix} |U|U \\ |V|V \\ |W|W \end{pmatrix}, \tag{19}$$

where f_i is force per volume, C_i the inertia loss term, D_i the viscous loss term, and the velocity components are U, V, W [19]. Large-scale settings are obtained with small scale CFD simulations by using the actual fabric structure introduced by Laakkonen [25, 26].

The permeability, velocity and structure changes of the fabric are considered as variables. The results and model description are shown in chapter 3.

2.4 *Computational fluid dynamics*

In this thesis, the CFD calculations are based on Reynolds averaged Navier-Stokes equations performed with a commercial CFD-software, ANSYS Fluent 6.3. A segregated pressure-based steady state solver has been used.

The flows near the rolls and fabrics in paper machines are boundary layer-driven. In the vicinity of the roll nips and inside the groove, the flow is turbulent and it is modeled by using a renormalized group theory (RNG) k-ε turbulence model. The selected turbulence model has been used in several sources, for example [1, 13, 14, 24, 25, 26]; therefore changes in turbulence modeling have not been considered. For complete details about the used solver and models, see [8].

In boundary layer -driven flows, the near wall treatment has to be considered carefully. For accurate calculation of the boundary layer, the enhanced near wall model is selected, where the viscosity-affected near wall region is computed completely, starting from the viscous sub layer. The flow domain is subdivided into a viscosity-affected region and a fully turbulent region. This is called a two layer model. The above mentioned regions are determined on the basis of the wall distance and turbulent Reynolds number Re_y defined as [8]

$$\mathrm{Re}_y = \frac{\rho y \sqrt{k}}{\mu}, \tag{20}$$

where y is the normal distance from the wall at the cell centre. Wolfstein's [52] one-equation model is used in the viscosity-affected near the wall region ($Re_y < 200$). For the fully turbulent region, the enhanced turbulent law ($Re_y > 200$) of the wall is used, which has been derived by combining the approaches of White and Cristoph [49] and Huang et al. [12].

The calculation mesh type in 2-dimensional simulations is quadrilateral, and in 3-dimensional it is hexahedral. When enhanced wall functions are used, high computation mesh resolution at the surface of the wall is needed. The boundary layer cells are used on the wall surfaces. In the nip areas, the mesh size starts from 0.001 m. Further away from the wall

surface, the mesh size can be increased with the factor 1.2. A typical computation mesh is shown In Figure 38 with nomenclature.

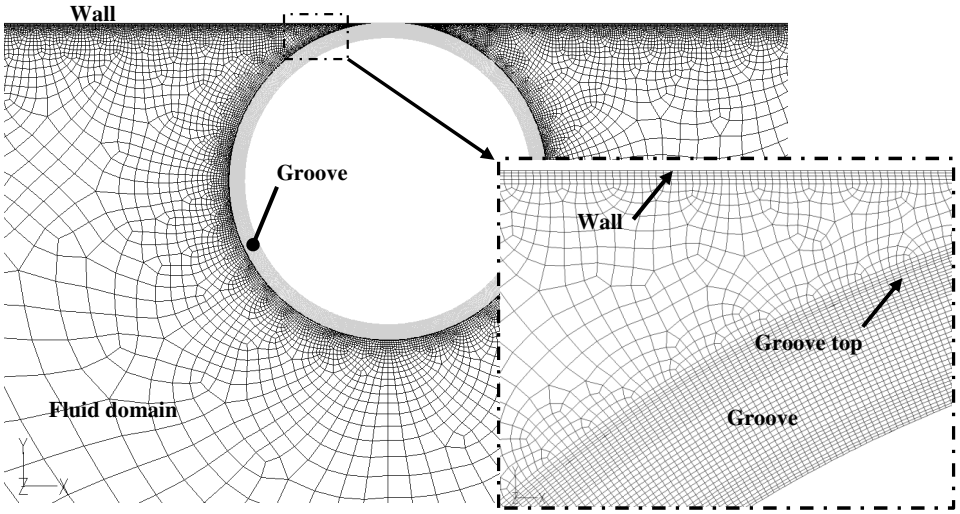

Figure 38: Typical mesh size in the grooved roll model.

Calculation mesh refinements have been done when necessary with a grid adaptation tool based on y^+ values suggested for a *k-e* turbulence model with enhanced wall functions [8]. The second order upwind discretization scheme has been used for the variables of pressure, momentum, turbulence and energy.

The 2D grooved roll simulation tool reduces the computational effort significantly. As a comparison, the 3D small wrap angle grooved roll model with mesh cell count 340k pcs reduces to a 2D grooved roll model with 79k cell count. This reduction in mesh size can be seen in the solving time. A simple test with the Linux operating system and one Intel 64-bit 2.6 Ghz processor PC platform showed that the solving time (10000 iterations) with the 3D grooved roll model was 15 hours 30 minutes and with the 2D grooved roll model 1 hours 45 minutes.

2.4.1 Convergence

Iterative convergence is monitored for all CFD models and it is achieved when at least three orders of decrease of magnitude in normalized residuals are observed. The mesh sensitivity check has been performed for the 2D grooved roll model. In the model, the groove effective height L_{eff} is 10 mm, $L_{g,w}$ and $L_{l,w}$ are 9 mm, and the radius r is R. The surface velocity v_x is

1500 m/min. The wrap angle of the horizontal wall over the grooved roll is small. The model is shown in Figure 29. The used mesh type is quadrilateral. The effect of the mesh size to solution convergence and accuracy in the grooved roll models has been tested with one 2D grooved roll model. Locally, in the groove and nip areas, the mesh size changes correlate with the overall cell count. With the finest mesh, the smallest cell size in the nip area is 0.3 mm. The tested mesh cell counts N are: N_1 122947 (fine), N_2 60908 (medium) and N_3 35836 (coarse) with the total area A of 20.01 m². The normalized residuals for continuity, momentum, energy and turbulence are shown in Figures 39*a*, *b* and *c*. The residuals show that convergence is achieved with the coarse mesh with less iteration cycles (< 5000 iterations). The medium mesh requires at least 13000 iterations, and the fine mesh 17000 iterations.

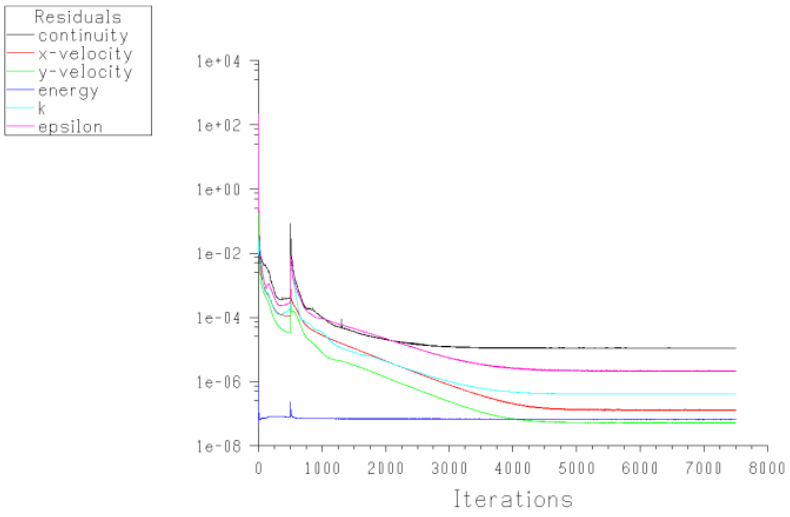

Figure 39: *a*) Coarse mesh,

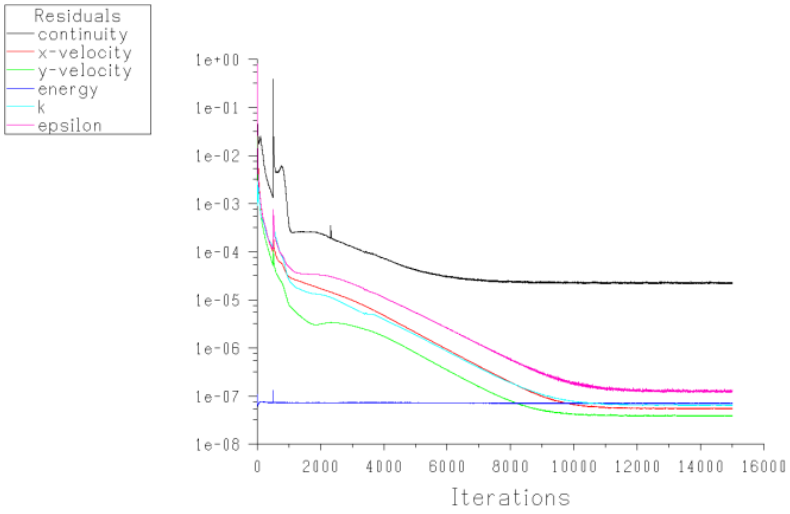

b) Medium mesh,

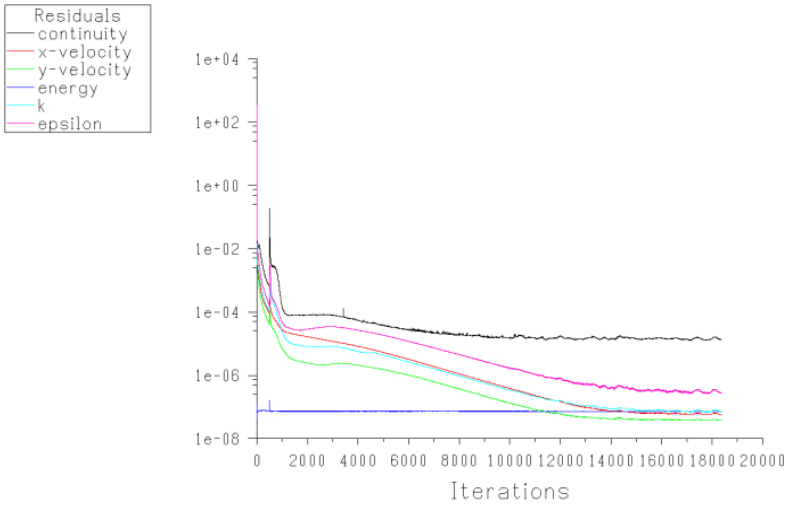

c) Fine mesh.

In the evaluation of grooved roll simulations, static pressure and air flow velocities in the groove are important variables. During the iterations, the magnitude of the static pressure and velocity at the tangent point of model was captured, shown in Figures 40*a* and *b*. The coarse mesh reaches the convergence level two times faster than the fine mesh solution.

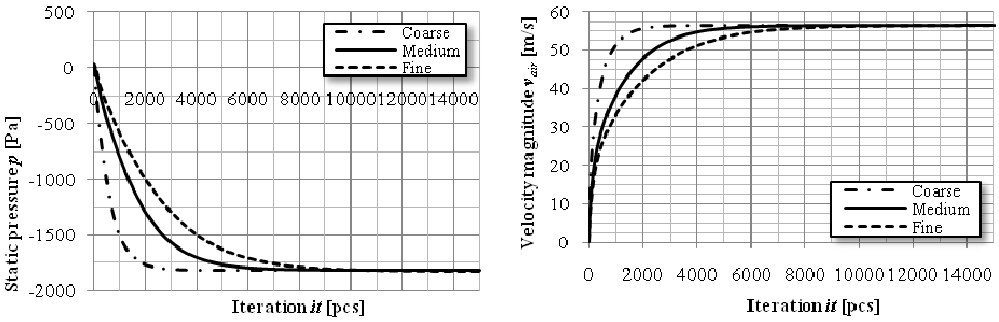

Figure 40: *a)* Static pressure at the tangent point, *b)* Air velocity at the tangent point.

The results for the mesh resolution variations are shown in Table 2. The static pressure difference between the coarse and fine meshes is 0.7%, and in the air velocity it is 0.2%.

Table 2: The effect of mesh resolution changes on the results.

Mesh resolution	***N* [pcs]**	***p* [Pa]**	v_{air} **[m/s]**
Coarse	35836	1813	56.38
Medium	60908	1814	56.38
Fine	122947	1826	56.47

2.4.2 Uncertainties due to discretization

Evaluation of discretization error is performed with the grid convergence index (GCI) method, which is based on the Richardson extrapolation (RE) method [3]. The evaluated meshes and variables were introduced in Table 2 in Section 2.4.1. The fine-grid convergence index GCI_{fine}^{21} between the medium and fine meshes is 0.2%, considering the static pressure as the variable. Based on the GCI index, iteration cycles and results, it is justified to use medium mesh accuracy. In this thesis, the mesh size has been chosen similarly as in the medium mesh.

3 MODEL VALIDATION

Validation of the grooved roll model is presented in this chapter. In order to ensure the functionality of the 3D and the 2D grooved roll models, model validation has been performed with laboratory scale measurements. A *grooved roll simulator* has been built for the measurements of pressure in the groove. The model validation consists of variations in the groove geometry, rotational speed and fabric permeability. The fabric wrap angle is kept constant. The measurements have been done with permeable fabric and taped impermeable fabric. The laboratory scale measurements have been done by Dr J. Leimu and his staff at Turku University of Applied Sciences (TUAS) in summer and autumn 2009. The author of this thesis has analyzed and compared the measurement results to the corresponding computational fluid dynamics models.

In Section 3.1, the experimental setup is presented, including information about the simulator geometry, pressure measurement devices and measurement procedure. Section 3.1.5 presents details about the selected test cases. In Section 3.2, the measurement results are compared to the computational fluid dynamics results. Section 3.3contains an evaluation of the measurement uncertainties.

3.1 *Experimental setup*

3.1.1 Simulator geometry

The grooved roll simulator consists of three support rolls, measuring equipment, an electric motor, fabric and the grooved roll. The rolls and the motor have been assembled together in a main frame. The fabric creates a closed loop around the support rolls and the grooved roll. The fabric tension can be controlled by changing the vertical position of the grooved roll. The fabric wrap angle over the grooved roll is adjustable when two lower support rolls are moved closer or apart from each other. At this point, it is not possible to construct the small wrap angle coverage over the grooved roll, due to simulator geometric limitations. The electric motor is connected to the upper support roll shaft. The transmission to the two lower support rolls and the grooved roll is delivered through the fabric. The fabric and roll velocities are controlled with an AC drive by changing the frequency of the motor power supply. The main

parts of the grooved roll simulator are shown in Figure 41 with nomenclature. In Figure 42, the grooved roll is shown as a photograph, clarifying the technical drawing.

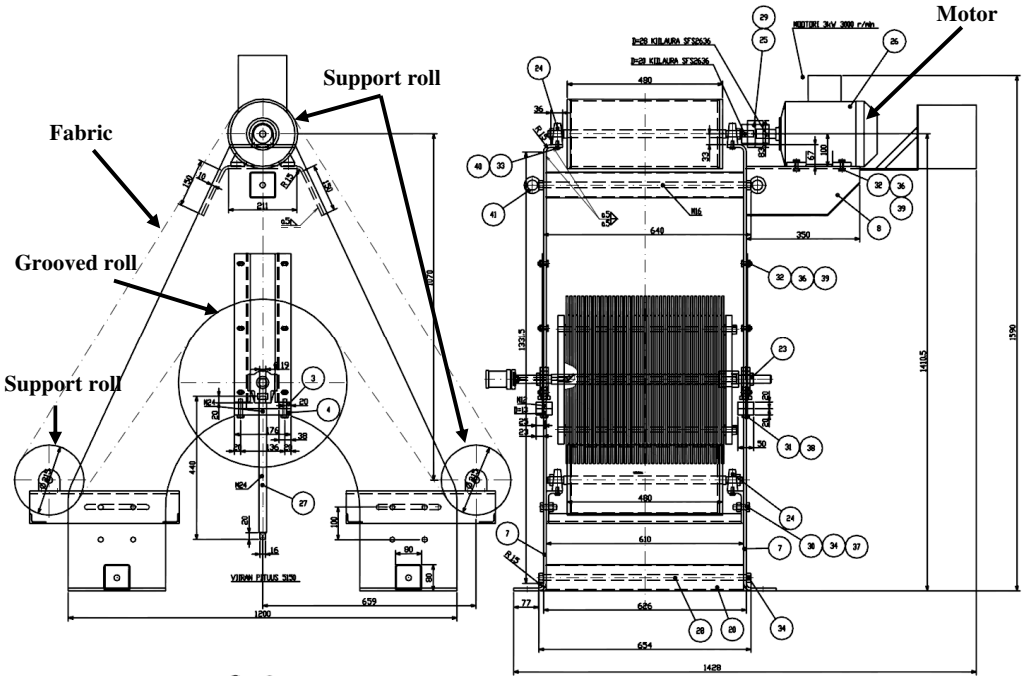

Figure 41: The grooved roll simulator. Figure courtesy of Metso Paper.

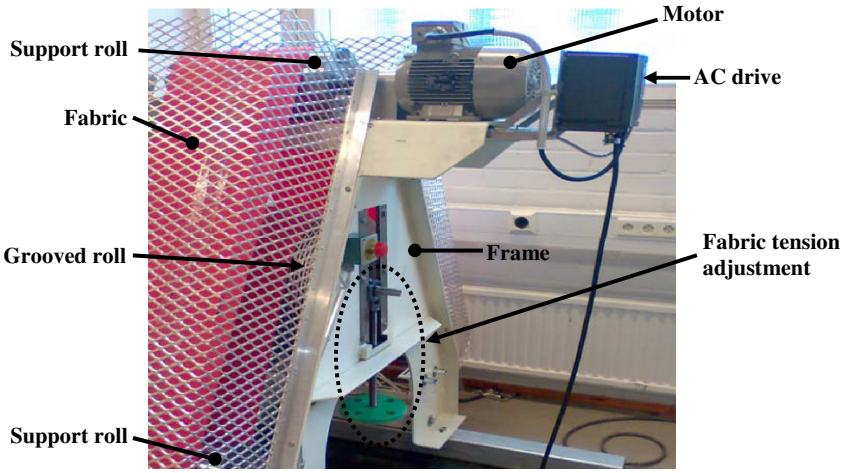

Figure 42: The grooved roll simulator. Figure courtesy of Miulus & Mattila/TUAS.

The grooved roll is made from aluminum plates, which are held together with six long bolts and end plates. The groove geometry can be varied by changing the plate thickness and radius. The grooved roll in the grooved roll simulator is shown in Figure 43.

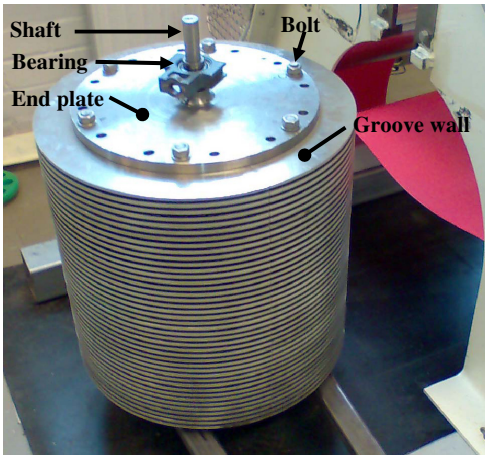

Figure 43: The grooved roll of the simulator. Figure courtesy of Miulus & Mattila/TUAS.

3.1.2 Groove pressure measurement

The purpose of the pressure measurement is to capture the pressure curves from the groove bottom as well as close to the roll land when the roll is rotating. The pressure measurement arrangement is similar to the one introduced by Kurki & Martikainen [22]. The pressure transducers are located in separate grooves, one close to the roll land attached to the roll wall and the other inside the groove bottom. The used miniature pressure transducers are *Kulite xcs-093*, calibrated after installation to the grooved roll. In Figure 44, pressure measurement from the groove bottom and roll land is shown schematically.

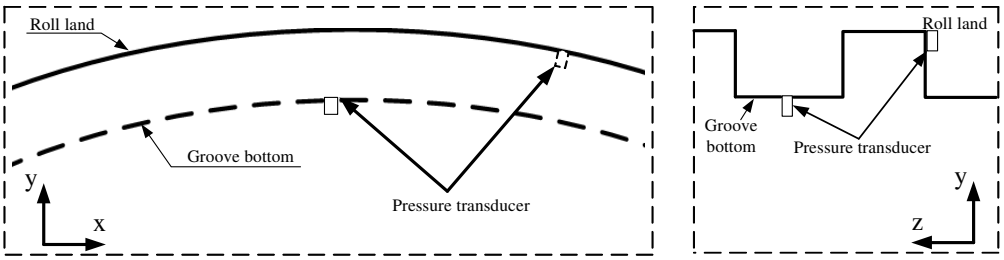

Figure 44: Pressure measurement configuration (ver. 2.0).

The electric signal measured with the pressure transducers is delivered through wiring to the grooved roll shaft, as shown in Figure 45*a*. On the other side of the shaft, the electric measurement signal is passed through the slide ring to a signal amplifier. The signal amplifier is connected to a data logger, which is able to capture the signal with 50 kHz sampling frequency. The slide ring and signal screen are shown in Figure 45*b*.

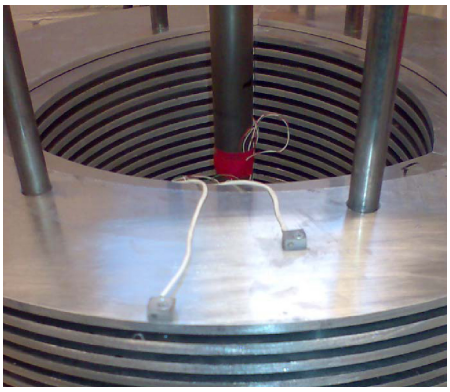

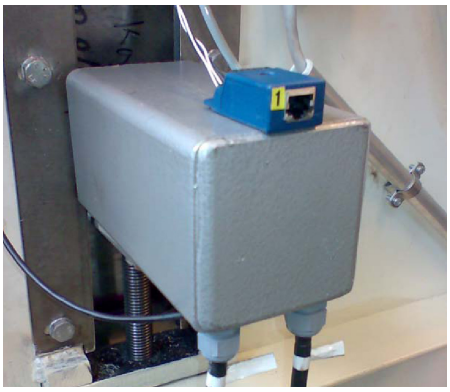

Figure 45: a*)* Pressure measurement transducers installed to the groove wall. Figure courtesy of Miulus & Mattila/TUAS, *b)* Slide ring at the end of grooved roll shaft. Figure courtesy of Miulus & Mattila/TUAS.

A trigger sensor is used to measure the grooved roll velocity and to locate the position of the pressure transducers relative to the nips and wrap angle. The trigger sensor is in the middle of the wrap angle, shown in Figure 46*a*. The measurement devices are able to capture static pressure as a function of one roll rotation. When triggering happens, the pressure transducers are 180° ahead between the opening and closing nips in the roll open area. The measured pressure curve is a function of the grooved roll outside circumferential length s_0. Figure 46*b* shows the triggering sensor and the pressure measurement path schematically.

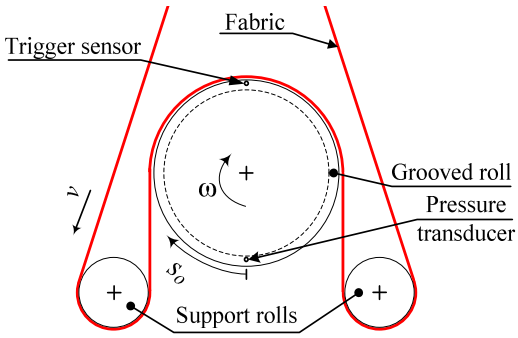

Figure 46: *a)* Trigger sensor. Figure courtesy of Miulus & Mattila/TUAS, *b)* Pressure measurement curve in the groove

The ambient temperature is monitored with a PT-100 thermo element attached to the main frame of the simulator.

3.1.3 Measurement procedure

When the desired geometry is assembled and all sensors are connected to the data logger, the measurement phase can start. The fabric and roll velocity are adjusted from the AC drive by changing the frequency of the electric motor power supply. After the startup and every velocity, it is recommended to wait for a couple of minutes to reach the stabilized flow conditions in the simulator. The measured data can be monitored and saved with a personal computer using Labview software. The fabric permeability changes are done by changing the fabric. The impermeable fabric condition is carried out by taping the groove side of the fabric with wide impermeable tape.

3.1.4 CFD models

The experimental setup, the grooved roll simulator is modeled with 3D and 2D grooved roll CFD models. The modeling details for 2D and 3D models were presented in Sections 2.2. and 2.3. The model geometry is identical to the simulator geometry. The roll distances, groove and roll dimensions and fabric properties are the same. The main difference to previous CFD models is the wrap angle and the use of the fabric as a moving surface. The used solver settings and turbulence models were presented in Section 2.4. The simulator CFD model with boundary conditions and nomenclature is shown in Figure 47.

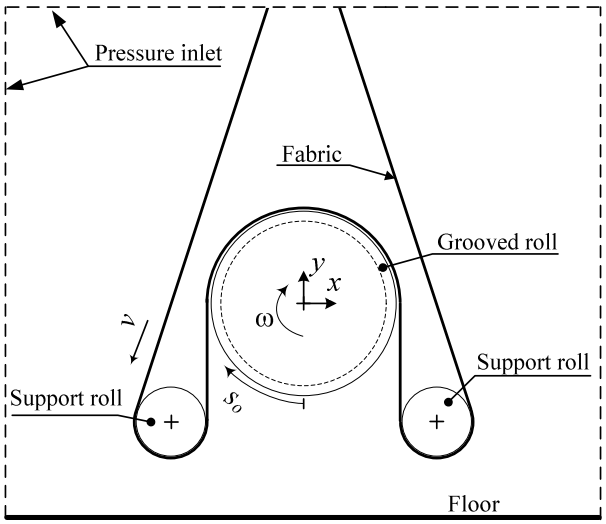

Figure 47: The simulator CFD model geometry with boundary conditions and nomenclature.

3.1.5 Test cases

The performed measurements are described in the following. The test cases are numbered in the following manner: the first case in Table 3: (1 1 0). The first number indicates the test set (1-8). The second number is velocity: 1 = 1200, 2 = 1600, and 3 = 2000 m/min. The third number indicates the wall permeability: 0 = impermeable or 1 = permeable. The other variables in the columns of table 3 are the grooved roll radius r, groove width $L_{g,w}$, roll land width $L_{l,w}$, groove height $L_{g,h}$ fabric permeability, and wrap angle α_{wrap}. The CFD models are shown in the last column. The case number 1 2 0 has been chosen as a reference case for an impermeable wall and 1 2 1 for a permeable wall. The groove and roll land widths are 6 mm, and the groove height is 20 mm. In the case of the permeable wall, woven fabric with permeability of 1800m/h is used. The simulator and CFD model grooved roll radius r is kept constant as 0.61R. The changes between the test cases are indicated by bolding and underlining the variable. In Table 3, examples of details in the measurement geometries are shown. A complete table of the test cases for the geometry and fabric property variations can be found in table 5 in APPENDIX A.

Table 3: Test cases for velocity variations with reference geometry.

Case	*r* [mm]	$L_{g,w}$ [mm]	$L_{l,w}$ [mm]	$L_{g,h}$ [mm]	*v* [m/min]	*Permeability* α [m/h]	*Wrap angle* [°]	*CFD model*
1 1 0	0.61R	6	6	20	**1200**	0	180	X
1 2 0	**0.61R**	**6**	**6**	**20**	**1600**	**0**	**180**	**X**
1 3 0	0.61R	6	6	20	**2000**	0	180	X

The fabric structure and permeability changes are considered as a variable. For the grooved roll aerodynamic functionality, the fabric permeability is an important property. In the following, the changes in the fabric structure and permeability are considered. The used groove geometry is the reference case 1 2 1. Woven and spiral fabric structures are tested in the simulator and in the CFD models. The fabric permeabilities are 1500, 8000 and 15000 m/h. Details about the fabric model and structures can be found in section 2.3.3. A complete table of the test cases for the fabric structure and permeability variations can be found in tables 6 and 7 in APPENDIX B.

3.2 *Results*

In the following, the simulation and measurement results are compared in order to validate the grooved roll simulation tool (GRT). The rotational pressure curves as a function of the roll circumferential length from the groove *bottom* and the groove *top* are under investigation. The circumferential length is divided to degrees marked with α_c. The closing nip is located at the place where α_c is 90° and the opening nip α_c is 270°. The pressure curves in the grooves are modified to dimensionless groove pressure p^* shown in Equation (21)

$$p^* = \frac{p}{p_{ref}}, \tag{21}$$

where p is static pressure and p_{ref} is the reference pressure. The measurement case 1 2 0 is the reference test setup for the CFD models and measurements. Details of the used geometries are presented in Appendices A and B. In the results, the CFD models are marked as follows: *2D* is the two-dimensional grooved roll model including GRT, *3D* is the three-dimensional grooved roll model, and the measurements with the grooved roll simulator are marked as *M*. The permeable fabric is *fabric* and the taped impermeable fabric is the *wall*.

The results section is divided to three subsections. Subsection 3.2.1 introduces the groove functionality when the groove dimensions, surface velocities and wall permeability are changed. The results are taken from the three-dimensional grooved roll models. In subsection 3.2.2, the 3D and 2D grooved roll models are compared. The grooved roll simulation tool (GRT) is used in this 2D model. Subsection 3.2.3 includes the measurement results made with the grooved roll simulator in the laboratory. The measurement results are compared to the 3D grooved roll simulation results.

3.2.1 Groove aerodynamic functionality

The grooved roll has to work in two different conditions due to changes in the fabric permeability. Normally the paper is attached to the fabric surface and air does not flow through the fabric. This situation is marked as *wall*. The condition when air is allowed to flow through the fabric is marked as *fabric*.

The 3D simulation results with cases 1 2 0 and 1 2 1 reveals a difference in pressure curves when the fabric permeability is changed. The dimensionless groove pressure $p^* = 0$ corresponds with the ambient pressure. Figure 48 depicts a comparison of groove bottom pressure distribution with wall and fabric condition presented. The closing nip is marked with *C* and the opening nip *O*. The wall and fabric wrap angle is between the closing and opening nips. The curve legend shown in the lower left hand corner indicates the cases and the used line types.

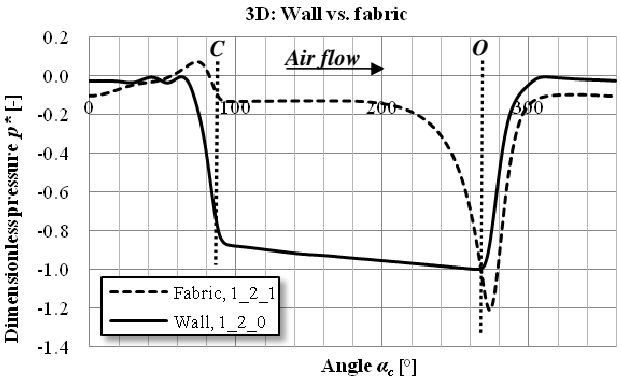

Figure 48: Comparison of pressure distribution in the groove bottom between the wall and the fabric.

The air flow friction losses have become more important due to the large wrap angle. The groove air flow friction losses can be seen as a pressure gradient in the continuous line in the wrap angle area. The air flow direction is from the closing nip to the opening nip. An analogy to pipe flow can be established. When the fabric is permeable, the closing nip overpressure and the opening nip underpressure are more local. The underpressure in the grooves does not increase due to leakage through the fabric. The boundary layer flow along the fabric surface and the groove causes overpressure to the closing nip, because the opening nip underpressure does not remove excessive air through the groove.

In Figures 49*a* and *b*, the closing nip air velocity vectors colored by the velocity magnitude, with wall (1 2 0) and fabric (1 2 1) boundary conditions, are shown. A difference in air velocities can be seen in the closing nip tangent point. In the fabric condition, the groove transports more air than the wall condition. Excessive air flows to the closing nip and partly through the fabric, causing overpressure into the closing nip, are seen in Figure 48.

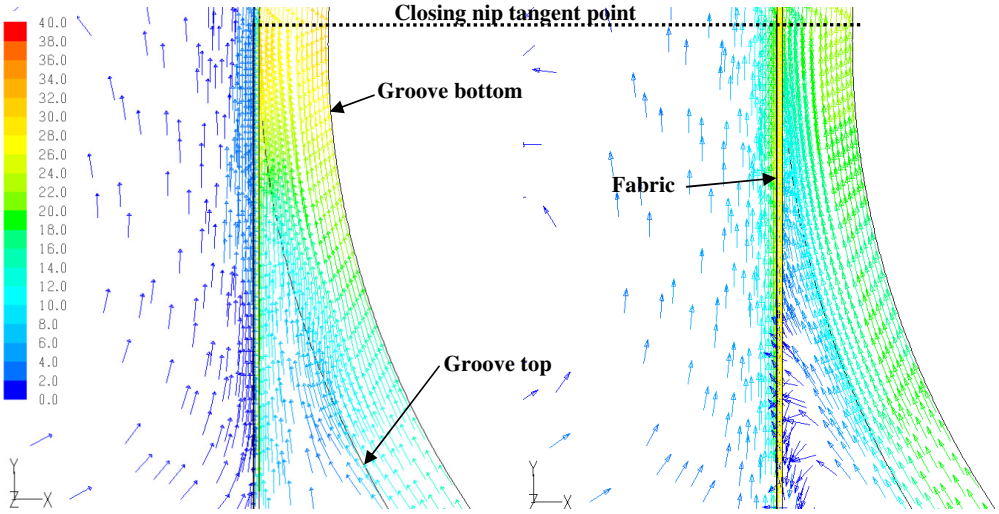

Figure 49: *a)* Closing nip velocity vectors with wall, *b)* Closing nip velocity vectors with fabric.

In Figures 50*a* and *b*, opening nip velocity vectors colored by the velocity magnitude, with wall (1 2 0) and fabric (1 2 1) boundary conditions, are shown. With the moving wall, the air flow follows the wall surface, emptying the groove and causing swirling, shown with the dotted line in Figure 52*a*. With the fabric condition, the air flow accelerates due to opening nip underpressure and follows the groove surface.

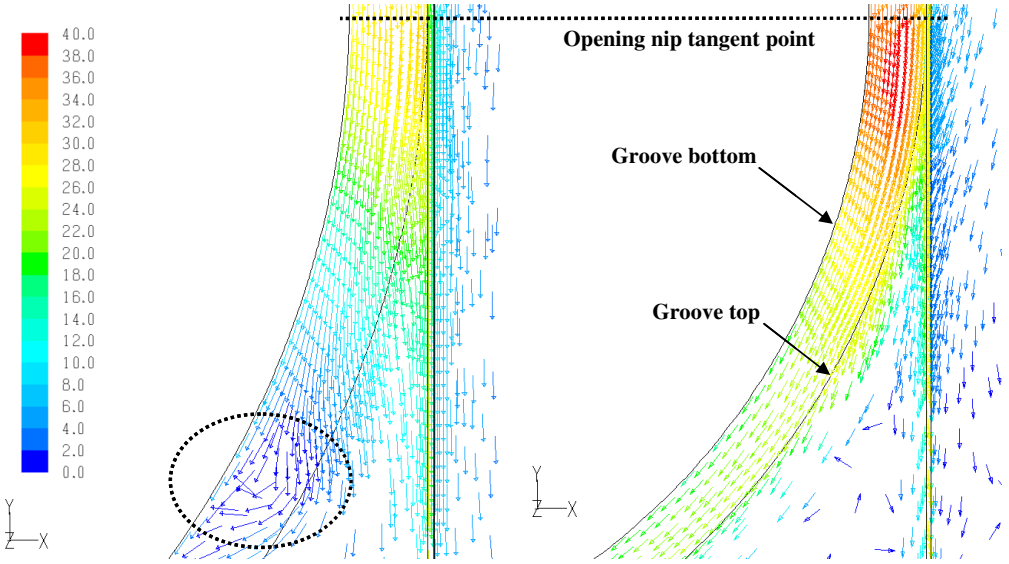

Figure 50: *a)* Opening nip velocity vectors with wall, *b)* Opening nip velocity vectors with fabric.

The pressure inside the groove varies as a function of roll radii. Figures 51*a* and *b* show pressure curves from the groove top and bottom with wall and fabric boundary conditions. In Figure 51*a,* the pressure in the wrap angle differs in the top and bottom curves. The fabric boundary condition indicates a pressure difference all the way between the top and the bottom. From the web handling point of view, the pressure at the groove top is the one which affects the paper web.

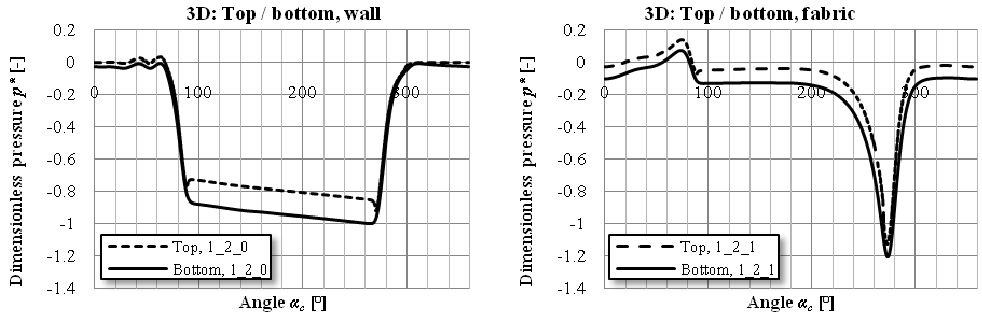

Figure 51: *a)* Comparison of pressure distribution between groove top and bottom with wall, *b)* Comparison of pressure distribution between groove top and bottom with fabric.

The groove underpressure is strongly affected by the surface velocity, similar to the small wrap angle simulations shown in Chapter 2. Pressure velocity dependency with the wall is

presented in Figure 52*a*. The closing nip changes smoothly from the ambient pressure to the groove underpressure. In Figure 52*b,* the pressure curves show how the surface velocities are changed with the fabric. As with the wall, the underpressure is increased in the groove wrap angle area. The closing nip overpressure remains almost constant.

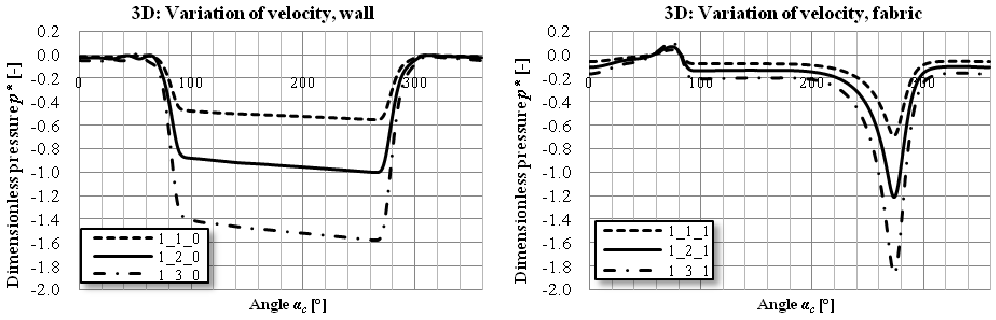

Figure 52: *a)* Effect of velocity *v* on pressure distribution with wall, *b)* Effect of velocity *v* on pressure distribution with fabric.

In Figures 53*a* and *b*, the groove depth is decreased from 20 mm to 10 mm. The groove cross-directional area lowers to half, which lowers the air volume flow through the groove. The closing nip pressure rises in both the wall and fabric cases. As a conclusion, the groove height of 20 mm produces a better result from the web handling point of view with a large wrap angle. The closing nip overpressure still remains in the tail threading case.

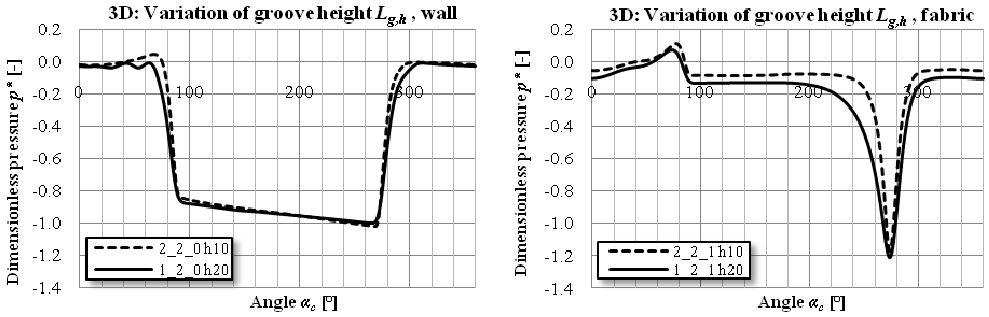

Figure 53: *a)* Effect of groove height on pressure distribution with wall, *b)* Effect of groove height on pressure distribution with fabric.

The test cases include roll land width $L_{l,w}$ variation from 6 mm to 10 mm, where the groove width $L_{g,w}$ is a constant 6 mm, the results of which are shown in Figures 54*a* and *b*. In the case of large wrap angles, the roll land width is not an important factor, compared to the case of the small wrap angle. The differences in the pressure curves are minor.

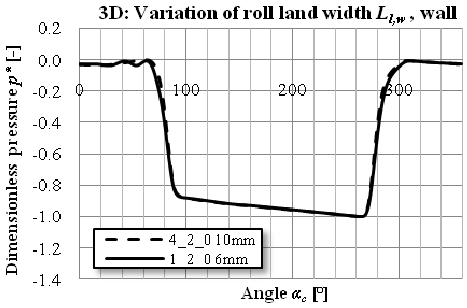

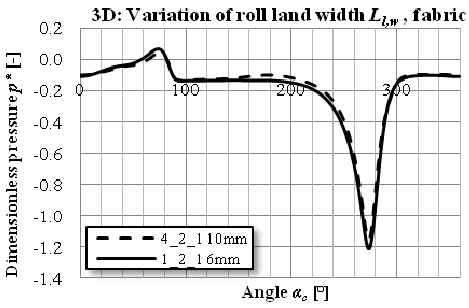

Figure 54: *a)* Effect of roll land on pressure distribution with wall, *b)* Effect of roll land on pressure distribution with fabric.

In Figures 55*a* and *b*, comparison of groove width $L_{g,w}$ changes from 6 mm to 4 mm is presented. Similar to the roll land variation, no significant changes in the pressure curves are observed. In this case, the groove fraction G_f changes from 0.5 to 0.4, which is a rather small change.

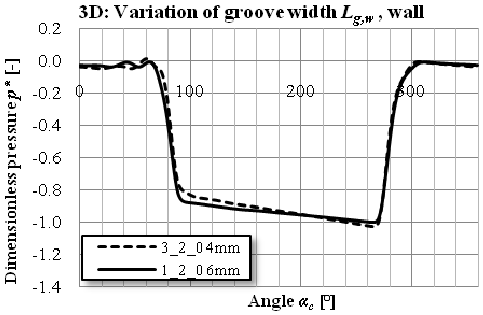

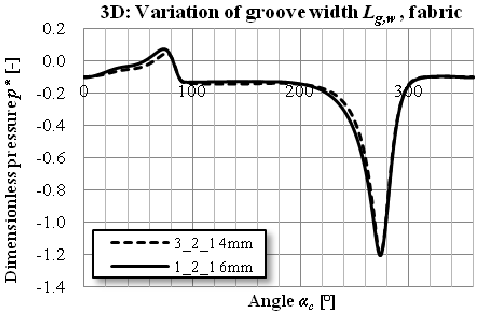

Figure 55: *a)* Effect of groove width on pressure distribution, *b)* Effect of groove width on pressure distribution.

The next three figures present the fabric permeability and structure changes. In Figure 56*a*, the fabric permeability is changed from 1800 m/h (1 2 1) to 1500 m/h (7 2 1), and 8000 m/h (8 2 1) in the woven fabric. Figure 56*b* presents the permeability change with the spiral fabric. The changed permeabilities are 1500 m/h (5 2 1) and 15000 m/h (6 2 1). With both fabric structures, the lower permeability produces slightly better underpressure to the wrap angle area than the reference case 1800 m/h. The down side for the lower permeability fabric is the closing nip overpressure. When the permeability is increased to be at least 3 times greater than in the reference case, the overpressure in the closing nip is at the same level but the opening nip underpressure area is smaller.

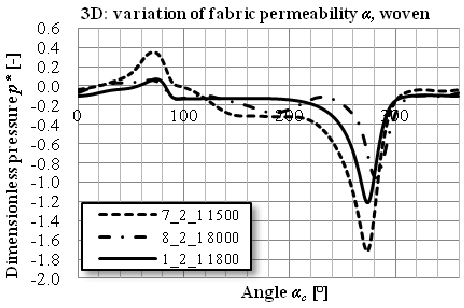

Figure 56: *a)* Pressure distribution in the groove when fabric permeability is changed with the woven fabric,

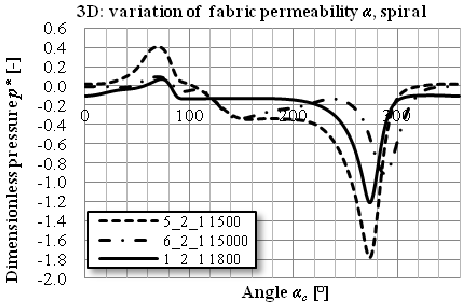

b) Pressure distribution in the groove when fabric permeability is changed with the spiral fabric.

In Figure 57, the effect of fabric structure is evaluated with the woven and spiral fabrics. In the selected cases, the fabric permeability α is 1500 m/h. The pressure curves are almost identical. On the basis of the closing nip overpressure, the woven fabric performs slightly better.

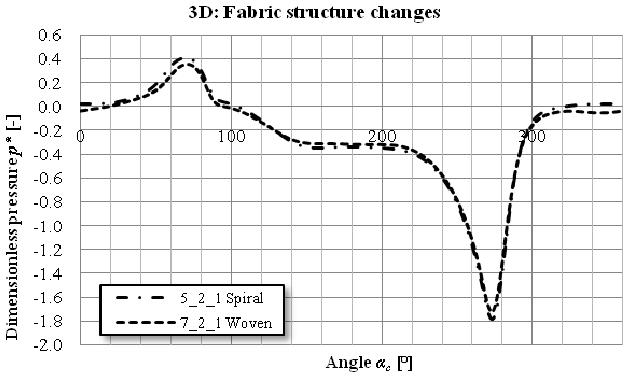

Figure 57: The effect of fabric structure on the pressure distribution in the groove bottom.

3.2.2 3D grooved roll model vs. 2D GRT model

In this section, the results of the 3D simulation model and the 2D GRT model are compared. The used geometry was introduced in Section 3.1. The GRT simplifications and the solution strategy for the 2D GRT model can be found in Section 2.3.

The 3D grooved roll models have been taken as the reference to which the corresponding 2D GRT models are compared. The air velocity v_{air} in the groove half way between the nips has been monitored in the 3D grooved roll models. The 2D GRT model porous jump

coefficient C_{2D} has been adjusted on the basis of air velocity in 3D grooved roll model $v_{air,3D}$ in order to reach the same air velocity $v_{air,GRT}$ in the 2D GRT model. It should be noted that for the fabric models, the porous jump coefficient is the same as with the wall model.

The air velocities in the grooves for the 3D and GRT model, as well as the porous jump coefficient are presented in Table 4. The air velocities reveal abnormality in the 2D GRT model. In geometry number 1, the porous jump coefficient is approximately 11. The geometry changes in the smaller groove show that the air velocity does not rise higher than in the corresponding 3D model, and the porous jump coefficient is set to 0. The air flows in the grooves with the wall boundary condition are laminar. The Reynolds numbers are less than 2300.

Table 4: Results of the 3D and GRT grooved roll models.

Case	C_{2D} [-]	$v_{air,3D}$ [m/s]	$v_{air,GRT}$ [m/s]	$v_{air,GRT} - v_{air,3D}$ [%]	$v_{rel,3D}$ [m/s]	Re [-]
1 1 0	11.0	21.52	21.53	0.02	1.52	1095
1 2 0	**11.0**	**28.82**	**28.82**	**0.00**	**2.16**	**1554**
1 3 0	11.1	36.15	36.15	0.02	2.82	2028
1 1 1	11.0	17.30	18.87	9.09	-2.70	
1 2 1	11.0	22.70	24.65	8.61	-3.97	
1 3 1	11.1	28.06	30.58	8.99	-5.27	
2 2 0	0	29.51	29.11	-1.36	2.84	1662
2 2 1	0	22.55	26.40	17.05	-4.11	
3 2 0	0	29.13	28.62	-1.76	2.47	1284
3 2 1	0	23.73	26.12	10.06	-2.94	
4 2 0	0	28.88	28.85	-0.08	2.21	1592
4 2 1	0	22.07	25.76	16.69	-4.59	

In Figures 58*a* and *b*, the 3D grooved roll and 2D GRT models are compared with the reference test setups 1 2 0 (wall) and 1 2 1 (fabric). In the wall wrap angle length, the pressure loss is 4 times larger than the one in the 3D grooved roll model. This observation points to the source term S used in the 2D grooved roll model, which might be overestimated. The closing nip overpressure behaves similarly in both the wall and fabric conditions.

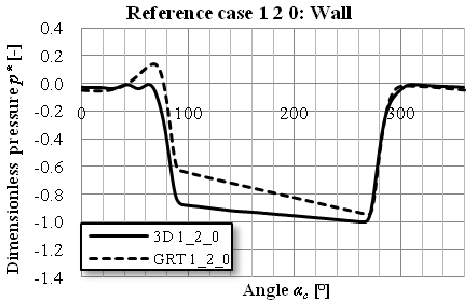

Figure 58: *a)* Pressure distribution in reference case 1 2 0 with wall,

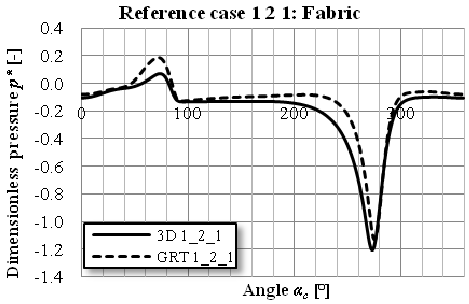

b) Pressure distribution in reference case 1 2 1 with fabric.

When the surface velocity is increased, the pressure levels are emphasized in the groove bottom. The effect of velocity increase to the 3D and 2D GRT models is presented in Figures 59*a* and *b*.

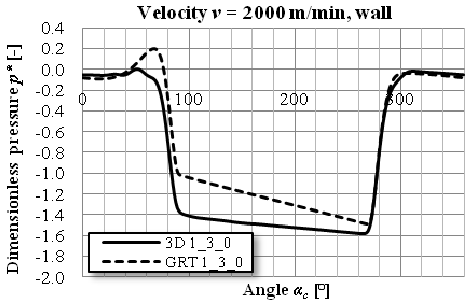

Figure 59: *a)* Effect of velocity *v* on pressure distribution with wall,

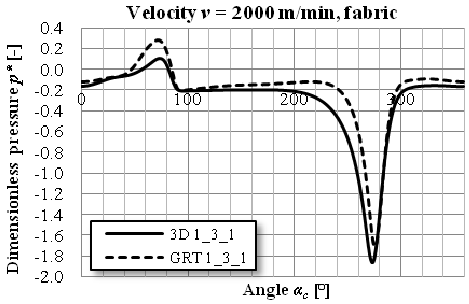

b) Effect of velocity *v* on pressure distribution with fabric.

In Figures 60*a* and *b*, the groove height has been lowered from 20 mm to 10 mm with the 3D grooved roll model and the 2D GRT model. The results are taken from cases 2 2 0 (wall) and 2 2 1 (fabric). In both situations, the GRT model overestimates the closing nip pressure, and the pressure gradient the groove at the wall wrap angle area. In these cases, the used GRT source term *S* is 30% higher than in the reference case 1 2 0.

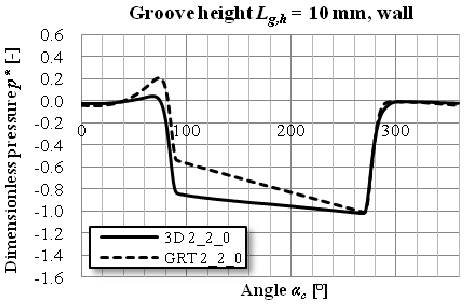

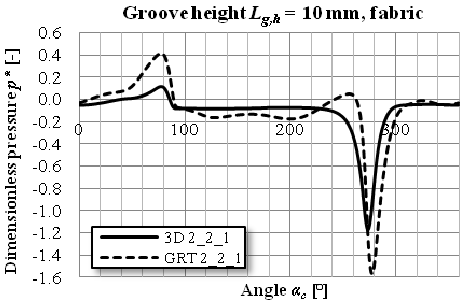

Figure 60: *a)* Effect of groove height on pressure distribution, *b)* Effect of groove height on pressure distribution.

When the groove width $L_{g,w}$ is decreased from 6 mm to 4 mm, and the roll land width $L_{l,w}$ is kept as 6 mm, the pressure gradients in the grooves are more drastic in the wall wrap angle area. The GRT friction source terms S are in this case on average 164% higher. In Figures 61*a* and *b*, the effect of groove width changes is shown with the wall and fabric boundary conditions.

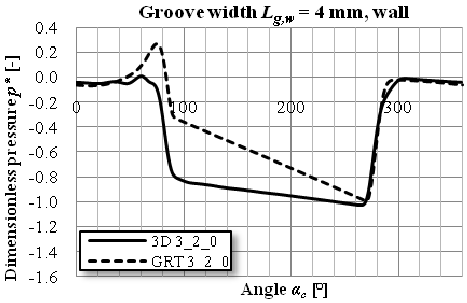

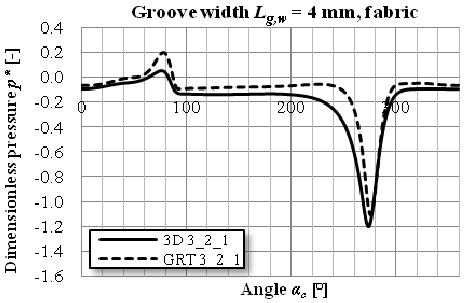

Figure 61: *a)* Effect of groove width on pressure distribution with wall, *b)* Effect of groove width on pressure distribution with fabric.

In Figures 62*a* and *b*, the roll land width $L_{l,w}$ is increased from 6 mm to 10 mm. In the case of a large wall wrap angle, the minor loss has only small influence on the total pressure losses which the air experiences when it flows through the groove.

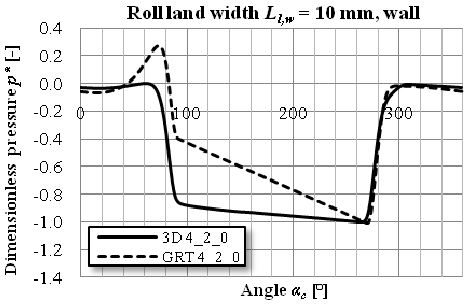

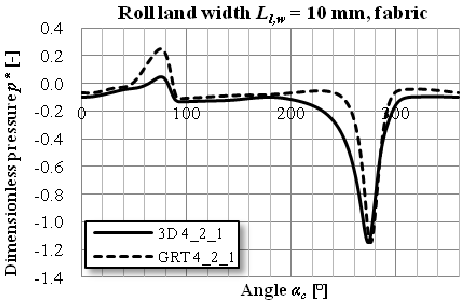

Figure 62: *a)* Effect of roll land width on pressure distribution, *b)* Effect of roll land width on pressure distribution.

The pressure distribution with woven and spiral fabrics with permeability α of 1500 m/h is shown in Figures 63*a* and *b*. The shapes of the pressure curves are almost identical between the fabric structures. Only small changes in the pressure levels can be observed. The GRT model underestimates the underpressure levels on both fabric structures.

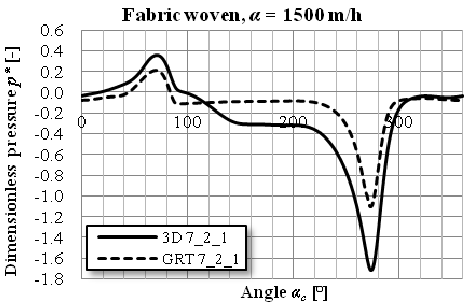

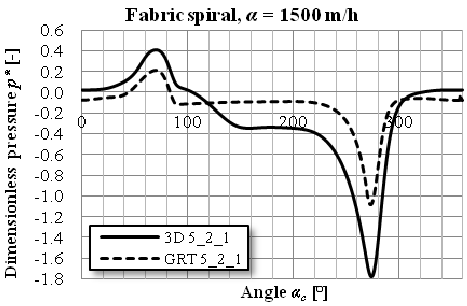

Figure 63: *a)* Pressure distribution in the groove with woven fabric with permeability α of 1500 m/h, *b)* Pressure distribution in the groove with spiral fabric with permeability α of 1500 m/h.

In Figures 64*a* and *b*, a comparison of the 3D and GRT models with highly permeable woven and spiral fabrics are shown. With the woven fabric, the pressure curves are identical in the opening nip. The 2D GRT model overestimates the pressure in the opening nip. The simulation results with the 2D GRT model and spiral fabric do not predict the pressure behavior well. The closing nip pressure is almost the same, but close to the opening nip, the pressure turns into overpressure.

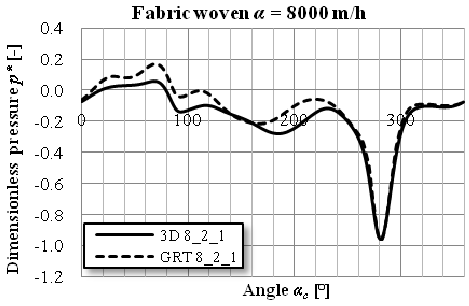

Figure 64: *a)* Pressure distribution in the groove with woven fabric with permeability α of 8000 m/h,

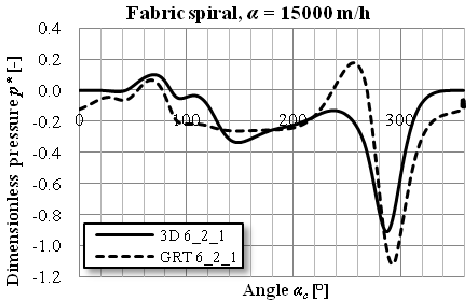

b) Pressure distribution in the groove with spiral fabric with permeability α of 15000 m/h.

As a conclusion of the simulations with the 2D GRT model, the used assumption of viscous losses calculated with pipe flow overestimates the pressure losses compared to the 3D grooved roll pressure losses. The 2D GRT model adds the groove bottom and wall surface viscous pressure losses even though they are included in the pipe flow viscous losses.

3.2.3 Comparison of the 3D grooved roll model and measurements

In this section, the results of the 3D simulation model and the measurements with the grooved roll simulator are compared. The used experimental setup was introduced in Section 3.1, including the description of the 3D grooved roll model and measurement procedure. In the following, the results of the measurements are marked with a continuous line and with the letter *M*. The pressure curves present the static pressure in the groove bottom unless indicated otherwise.

The measured pressure curves follow the pressure curves of the 3D grooved roll model. In the closing nip, the measurement shows a small overpressure compared to the 3D grooved roll model, as shown in Figure 65*a*. Between the nips (90° - 270°), the pressure fluctuates in the measurement pressure curve. The measurement indicates overpressure in the opening nip, which differs from the 3D grooved roll model results. The measurement with the fabric boundary condition, shown in Figure 65*b*, estimates the same pressure in the closing nip as the 3D grooved roll model. Only small differences can be observed in the pressure curves.

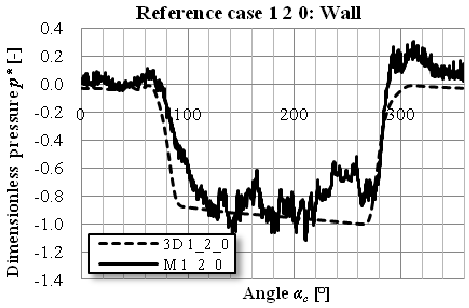

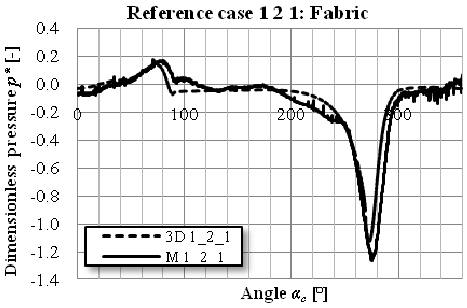

Figure 65: *a)* Pressure distribution of the 3D grooved roll model and measurements with case 1 2 0, *b)* Pressure distribution of the 3D grooved roll model and measurements with case 1 2 1.

The pressure distributions with the measurements and the 3D grooved roll model are shown in Figures 66*a* and *b*. When the velocity is 2000 m/min, the pressure level in the groove lowers to -0.4 with the dimensionless pressure p^* scale. The pressure fluctuation in the wall wrap angle reduces in the case 1 3 0. The case 1 3 1 with the fabric behaves similar to the case 1 2 1.

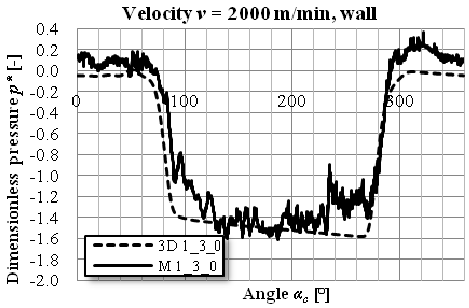

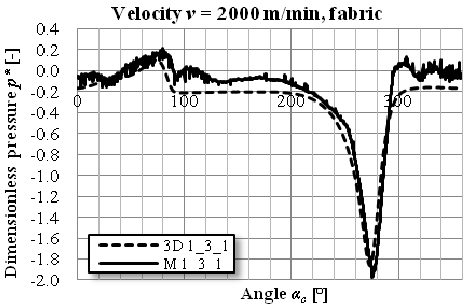

Figure 66: *a)* Effect of velocity *v* on pressure distribution with wall, *b)* Effect of velocity *v* on pressure distribution with fabric.

Fabric structure and permeability changes are considered as variables in the validation of the grooved roll models. The pressure distributions with spiral and woven fabrics with 1500 m/h permeability are shown in Figures 67*a* and *b*. Both measured pressure curves have similar shapes, even though the pressure levels are slightly different. In the closing nip, the 3D grooved roll model overestimates the pressure 0.2 with both models. In the fabric wrap angle area the measurement indicates small underpressure; it is mostly close to zero. In the opening nip, the underpressure with the spiral fabric is -1.4 and with the woven fabric it is -1.2. The 3D grooved roll models predict approximately the same opening nip -1.8

underpressure. With the woven fabric the pressure is more in the overpressure side than with the spiral fabric. The measurements with spiral and woven fabrics predict the highest underpressure at 278° which is approximately 5° more than what the 3D grooved roll model predicts. A possible reason for the shift is the movement of the opening nip tangent point due to high underpressure in the groove and low tension in the fabric.

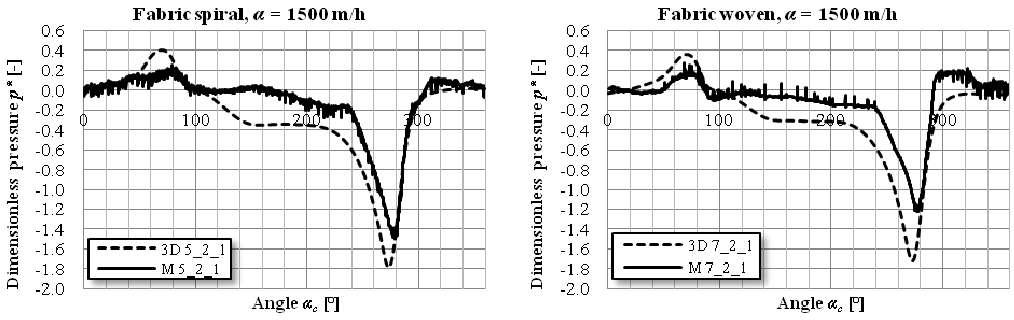

Figure 67: *a)* Pressure distribution with spiral fabric, *b)* Pressure distribution with woven fabric.

A comparison of the 3D grooved roll and measurement with the woven fabric with permeability 8000 m/h (Figure 68*a*) and with the spiral fabric with permeability 15000 m/h (Figure 68*b*) reveals that pressure distribution in the wrap angle area is similar to the fabric with 15000 m/h permeability. The shapes of the pressure curves are similar in the 3D grooved roll model and the measurements. The overpressure before the closing nip with the spiral fabric, shown in Figure 68*a* and Figure 67*b* with dotted ovals, is enhanced by the boundary layer flow at the fabric surface moving upwards (see Figure 47 for details).The woven fabric with the permeability of 8000 m/h gives higher underpressure than the spiral fabric with the permeability of 15000 m/h.

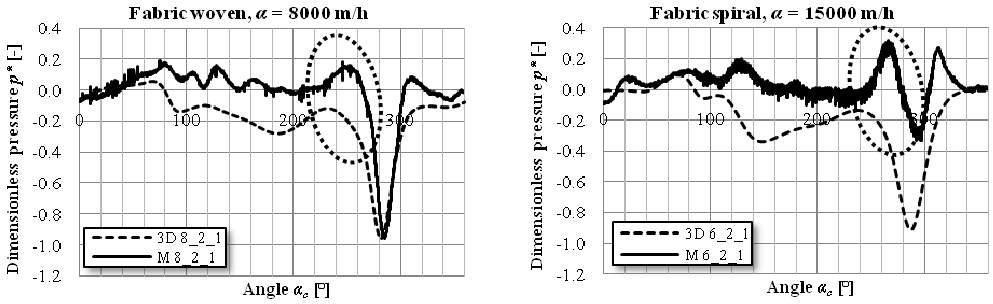

Figure 68: *a)* Pressure distribution with woven fabric, *b)* Pressure distribution with spiral fabric.

The reduction of the groove height to 10 mm lowers the closing nip overpressure with the fabric boundary condition compared to the reference case (1 2 1). The results of the 3D grooved roll model and measurements, shown in Figure 69*a* and *b*, are in reasonable agreement. Only notable differences between the 3D grooved roll model and measurement are in the pressure level in the groove open area (0°-80° and 290°-360°), shown with dotted ovals in Figure 68*a*.

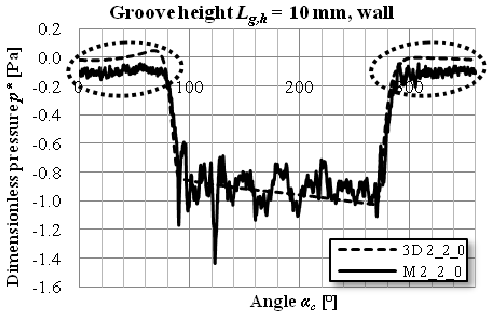

Figure 69: *a)* Effect of groove height on pressure distribution with wall,

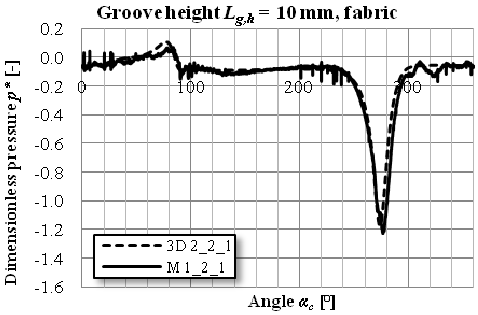

b) Effect of groove height on pressure distribution with fabric.

The groove width reduction to 4 mm increases the closing nip overpressure with the fabric boundary condition, shown in Figure 69*b*. The source of the ripple in the wrap angle area pressure curve may come from the electric interference in the measurement setup. The 3D grooved roll model and measurements show similar results in the wrap angle area in both the fabric (Figure 70*b*) and wall (Figure 70*a*) case. Pressure level differences of 0.1 can be found in the groove open area

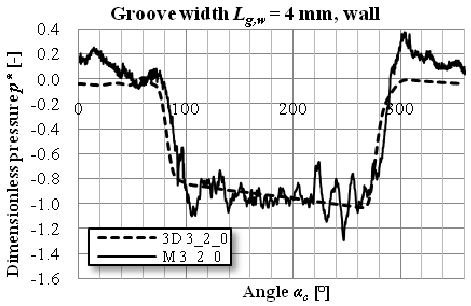

Figure 70: *a)* Effect of groove width on pressure distribution with wall,

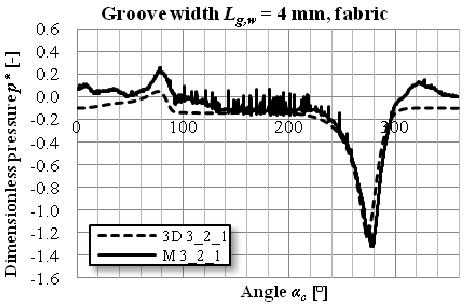

b) Effect of groove width on pressure distribution with fabric.

The pressure distribution with wall and fabric boundary conditions and 10 mm roll land width is shown in Figures 71*a* and *b*. Comparison between the 3D grooved roll models and measurements are presented. The measurement with the wall boundary condition, shown in Figure 70a, presents similar pressure levels in the closing nip and wrap angle. The pressure after the closing nip differs from the 3D grooved roll model pressure. The fabric condition, shown in Figure 70*b*, has similar positive pressure after the opening nip. This measurement differs from the previous results with different grooves and fabrics. The pressure level in the wrap angle area is in the positive side.

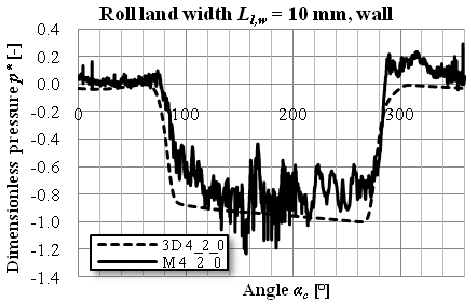

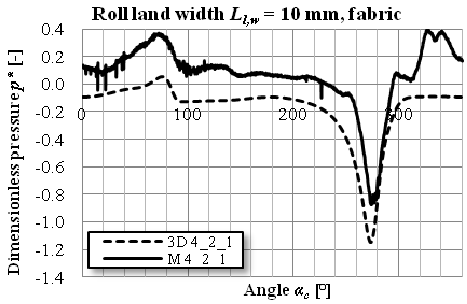

Figure 71: *a)* Effect of roll land width on pressure distribution with wall, *b)* Effect of roll land width on pressure distribution with fabric.

As a conclusion of the validation of the 3D grooved roll simulation model with the corresponding measurements the results are in good agreement with the wall boundary condition. The results with the fabric boundary condition have a few exceptions between the 3D grooved roll simulation results and measurements in pressure levels and pressure distributions.

3.2.4 Considerations on pressure measurements techniques

The 3D grooved roll model validation with the measurements sets a challenge for the measurement devices, due to high speeds and the rotating roll. When the measurements were started, the pressure transducers were attached to the groove wall, one close to the roll land and the other one close to the groove bottom. The first pressure measurement configuration is shown in Figure 71.

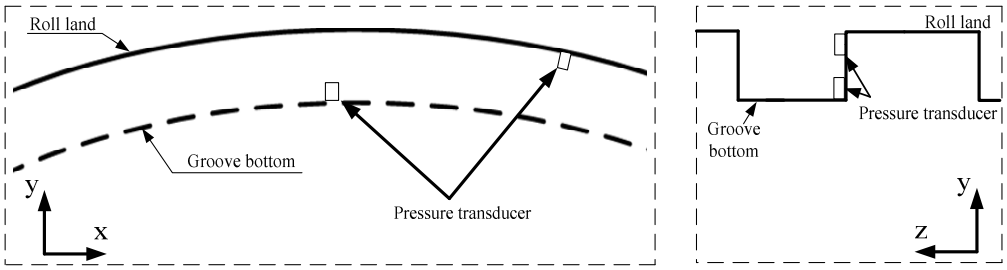

Figure 72: The first pressure measurement configuration (ver. 1.0).

The transducers were installed into the same groove with 10 degree phase change. The pressure transducer dimensions (5 x 9.5 x 2.4 mm) and the installation might be one reason for the fluctuation, causing local disturbance. The transducers caused pressure loss to the air flow through the groove. The groove bottom pressure transducer measured the pressure 10 mm from the bottom. The measurement results pointed out differences between the measurements and the 3D grooved roll model, which raised questions. It was decided to modify the measurement configuration in order to minimize the disturbances caused by the pressure transducers. The roll land pressure transducer was moved to the next groove wall. The groove bottom pressure transducer was mounted into the groove bottom. This way the groove remained free of extra pressure loss sources. The version 2.0 pressure measurement configuration is shown in Figure 43. In the following, examples are shown of the differences between version 1.0 and 2.0 measurements.

In the wall boundary condition, the pressure curve has larger fluctuation in the wrap angle area with the version 1.0. The measurement pressure curve indicates swirl in the opening nip, marked with the dotted line in Figure 73*a*. The swirl is shown in Figure 50*a,* with the help of velocity vectors. Closing nip pressure curves are similar in both measurement configurations. The opening nip side pressure seems to be at a higher level with the version 2.0 pressure measurement configuration. In the wrap angle area, the pressure level approaches the 3D groove roll model curve in the version 2.0 pressure measurement configuration. In Figures 73*a* and *b,* the pressure distribution in the 3D grooved roll model and the measurements in versions 1.0 and 2.0 are shown.

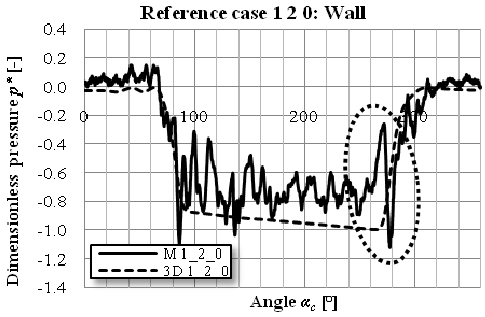

Figure 73: *a)* Pressure distribution of the 3D grooved roll model and measurements in case 1 2 0 (ver. 1.0),

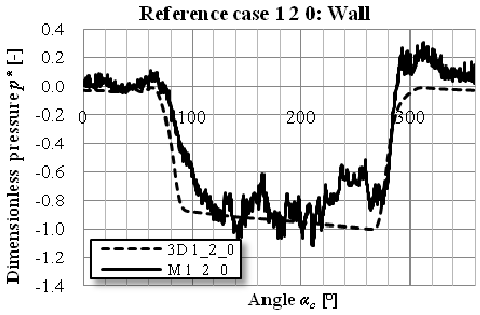

b) Pressure distribution of the 3D grooved roll model and measurements in case 1 2 0 (ver. 2.0).

The measurement with the fabric boundary condition, shown in Figures 74*a* and *b*, estimates the same overpressure in the closing nip as the 3D grooved roll model. Differences can be observed in the wrap angle area and in the opening nip. In the wrap angle area the pressure is slightly at a higher level in the pressure measurement version 1.0. The problematic area is in the opening nip. The pressure measurement with version 1.0 estimated the highest underpressure in the opening nip at 262° and in the 3D grooved roll model at 275°. A reason for the shifting was the pressure transducer dimensions blocking the groove air flow when the pressure transducer approach the opening nip.

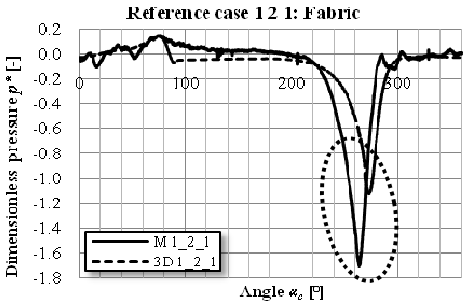

Figure 74: *a)* Pressure distribution of the 3D grooved roll model and measurements with case 1 2 1. (ver. 1.0),

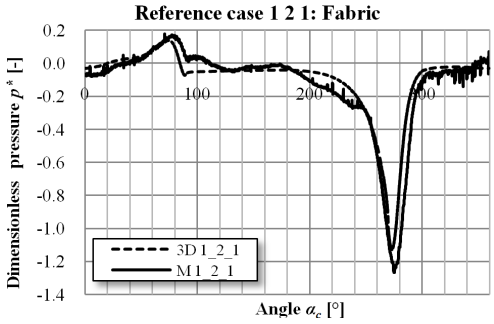

b) Pressure distribution of the 3D grooved roll model and measurements with case 1 2 1 (ver. 2.0)

As a conclusion, the version 2.0 pressure measurement configuration improved the results. The pressure distribution with the 3D grooved roll model and the measurements are now closer to each other, and the performed analysis enhances the reliability of the results.

3.3 *Measurement uncertainty*

Evaluation of the measurement uncertainty is based on the assumption that the ambient temperature is constant and conversion of the electric pressure message to pressure units is negligible. The uncertainties in signal transfers through the wirings are not taken into account. The three main components: pressure transducer, strain gage amplifier, and A/D converter influence the pressure measurement signal, causing uncertainties. The measurement signal cycle is shown in Figure 75.

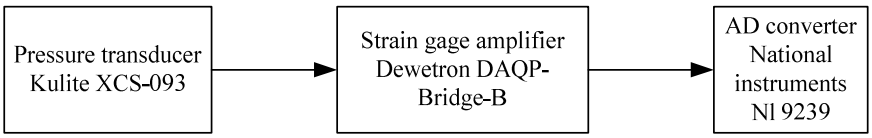

Figure 75: Measurement signal cycle.

The pressure transducer has uncertainties of non-linearity and hysteresis ε_{nlh} = 0.15 % and acceleration sensitivity ε_{accs} = 0.0015 % [20]. The thermal sensitivity shift ε_{tss} and thermal zero shift ε_{tzs} are 0 %, due to the assumption of constant temperature during the measurements [20]. Uncertainties coming from the strain gage amplifier are excitation voltage accuracy ε_{eva} = 0.05 % and excitation voltage drift ε_{evd} with 10 K temperature rise in the amplifier being 0.01 % [4]. The A/D converter measurement uncertainty ε_{adc} is defined as in Equation (22)

$$\varepsilon_{adc} = \frac{U_{fs,adc} \big/ N_{adc}}{U_{fs,ps} \cdot k_{amp}} \cdot 100\% \quad , \tag{22}$$

where $U_{fs,adc}$ = 20 V is A/D converter full scale voltage, $N_{adc} = 2^{24}$ is resolution, $U_{fs,ps}$ = 100 mV is pressure transducer maximum output value and k_{amp} = 50 is strain gage amplification. Based on the above mentioned uncertainties, the measurement uncertainty is shown in Equation (23)

$$E_T = \sqrt{(\varepsilon_{nlh})^2 + (\varepsilon_{tzs})^2 + (\varepsilon_{tss})^2 + (\varepsilon_{accs})^2 + (\varepsilon_{eva})^2 + (\varepsilon_{evd})^2 + (\varepsilon_{adc})^2} \approx 0.2\% \tag{23}$$

4 DISCUSSION

The aerodynamic behavior of the grooved roll was studied in this thesis by using computational fluid dynamics tools as the research tool. The closing and opening nip air flows were studied with smooth roll CFD models in order to understand the pressure development phenomena. The motivation for the grooved roll project was to find a replacement for the vacuum roll construction. The desired feature for the grooved roll is minimizing the closing nip overpressure and keeping the paper attached to the fabric in the roll wrap angle area. For the point of view of numerical simulations, the present-day computational and modeling resources limit detailed modeling of grooved rolls in paper machine scale simulations. A grooved roll simulation tool was proposed in this thesis. The numerical models were validated with a grooved roll simulator in laboratory scale measurements.

Karlsson's theory [18] predicts pressure changes in the closing nip when the boundary layer development length is changed. On the basis of smooth roll simulation models, the closing nip pressures do not change when the boundary layer development length is changed. The closing nip backflow disturbs the boundary layer flows in the nip area, and therefore the pressure in the nip does not change. The velocity profiles in the closing nip in the present study showed that changes in the boundary layer development length could be observed when $\alpha_{in} > 10°$. The backflow origin was at α_{in} 3°- 4°. When the surface velocity is increased, the air flow turbulence in the closing nip moves outwards. In this thesis, the closing and opening nips were solved as coupled for the first time. The influence of opening nip on the closing nip could be observed in the pressure curves of smooth roll simulation models.

In this thesis, a three-dimensional grooved roll model was used to study the aerodynamic functionality of the grooved roll. The basic condition is that the groove is covered partly with an impermeable wall (*wall, paper or web*). The air flow experiences viscous and minor losses when traveling through the nips and the groove. The groove dimensions affect these pressure losses. The viscous losses depend on the groove cross-sectional area and the minor losses on the groove fraction. The surface velocities of the wall and roll enhance the boundary layer flows. The closing nip forces the boundary layer flow into the groove, and the opening nip absorbs the air out from the groove. For this reason, the air velocities in the grooves grow higher than the roll surface velocity, causing underpressure into the groove. The grooved roll functionality changes when a small or large wrap angle is used. In the case of a small wrap

angle, the groove viscous loss has a smaller effect compared to the large wrap angle. With the large wrap angle, the pressure gradient caused by the viscous losses can be observed in the dominant pressure curves. A 3D grooved roll model was taken as a reference case to evaluate measurements and a 2D grooved roll model.

A 2D grooved roll simulation tool (GRT) was proposed in this thesis. The groove viscous losses were modeled in a 2D grooved roll by using the source terms. The viscous losses were calculated according to the basic pipe flow theory. The minor losses were described in the 2D grooved roll model with the porous jump boundary condition. A comparison of the simulation results between 3D and 2D grooved roll models revealed that the 2D grooved roll model predicted the air flows and the pressure distribution in good agreement with the small wrap angle. In the case of the large wrap angle, the source terms describing viscous losses were too large with the 2D grooved roll model. The pipe flow theory takes into account the groove wall friction on all sides. The 2D grooved roll model adds the groove bottom and top friction, and these walls are present in the model. Additionally, the groove top and bottom area increases with factor $1/G_f$ in the 2D grooved roll model compared to the 3D grooved roll model. In future model development, the 2D model groove top and bottom friction has to be taken into account.

The grooved roll models were validated with laboratory scale measurements. A grooved roll simulator was built to study the pressure distribution in the grooves when the roll rotates at high speed. The measurements were made with a large wrap angle. The measurement results were compared to the 3D grooved roll simulation results. When the grooved roll was covered with a wall, the simulations and measurements were in good agreement. The closing and opening nip pressure curves followed each other. In the wrap angle area, there was relatively small difference in the pressure distribution between the measurements and the 3D grooved roll model. The measurement showed pressure fluctuation in the wrap angle area. The 3D grooved roll model describes the flow condition in the middle of a very wide grooved roll, and the cross directional air flows are not taken into account. The simulator includes the cross directional flows, which might affect the closing and opening nip pressure levels.

When a fabric was used to cover the roll, more differences could be seen. The closing nip overpressure was estimated similarly in the measurements and the 3D model. The measurement uncertainties were estimated to be 0.2%, based on measurement device

accuracies. The installation of a roll land pressure transducer may have influenced the air flows due to the size of the pressure transducer. Fabric tension was not controlled with tension measurement, which may have affected the fabric permeability properties and the wrap angle.

5 CONCLUSIONS

The grooved roll has potential to replace the widely used vacuum roll construction from the aerodynamical point of view. The grooved roll is able to remove the boundary layer flow into the groove, and the closing nip overpressure is in control. With large wrap angles, the groove is in underpressure due to air flows in the groove. The grooved roll operates differently with large or small wrap angles; therefore the groove dimensions need to be optimized according to the web handling application and desired pressure levels.

The grooved roll simulation tool (GRT) will speed up and simplify the modeling work. The tool makes it possible to simulate large and complex parts of paper machines. The results obtained with the small wrap angle 2D grooved roll model were in a good agreement with the corresponding 3D grooved roll simulation. The source terms used to describe the viscous losses in the groove need to be reconsidered, which was observed in the 2D grooved roll simulation results with the large wrap angle.

In future development work, the focus will be on the expansion of the grooved roll simulation tool to a full 3D grooved roll simulation tool including side leakage and cross-directional air flows. The possibility to measure the small wrap angle of the wall or fabric with the grooved roll simulator could give more support to the future development work. In this research, heat and mass transfer and fluid structure interaction simulations were not included in the grooved roll models, but in the future this could be a useful option in large scale paper machine simulations.

REFERENCES

[1] Bergström, F., Åkerholm, J., Hansson, R., Möller, R.: Web drying simulations based on computational fluid dynamics. IX Finnish Mechanical Days, Lappeenranta, Finland, 2006

[2] Brafford Donald A, 20.4.1971. *Groove Roll Composition*. CA868689 (A) Beloit Corp

[3] Celik, I., Ghia, U., Roache, P., Freitas C.: Procedure for estimation and reporting of uncertainty due to discretization in CFD applications. Journal of Fluid Engineering, 130: 078001 (2008)

[4] Dewe modules. [www-document], [Retrieved October, 1 2009]. From: http://download.dewetron.com/_media//files/products/signal/daqp/manuals/dewe-modules_techref_223e.pdf

[5] Ducotey, K., Good, J.: A numerical algorithm for determining the traction between a web and a circumferentially grooved roller. Journal of Tribology, 122:578-584 (2000)

[6] Ducotey, K., Good, J.: The effect of web permeability and side leakage on the air film height between a roller and web. Journal of Tribology, 120:559-565 (1998)

[7] Fagerholm, L.: Aerodynamical properties of dryer fabrics for high speed paper machines. TAPPI Engineering Conference , Seattle, USA, 1990.

[8] Fluent Inc.: Fluent 6.3 User's Manual (2006)

[9] Hashimoto, H., Hikita, S.: Improvement of slippage and wrinkling of transporting webs using micro-grooved rollers. Proceedings of 10th International Conference on Web Handling, Stillwater, Oklahoma USA, 2009.

[10] Hashimoto, H., Okajima, M.: Theoretical and experimental investigations into spacing characteristics between roller and three types of webs with different permeabilities. Journal of Tribology, 128:267-274 (2006)

[11] Hashimoto, H.: Air film thickness estimation in web handling processes. Journal of Tribology, 121:50-55 (1999)

[12] Huang, P., Bradshaw, P., Coakley, T.: Skin Friction and Velocity Profile Family for Compressible Turbulent Boundary Layers. AIAA Journal, 31(9):1600-1604 (1993)

[13] Immonen, E., Bergström, F., Nurmi, S., Lehtinen, A., Juppi, K., Martinsson, L.: A 2D FSI model for small deflections of fast paper webs moving in geometries containing nips and boundaries. Proceedings of Paper Making Research Symposium (PRS 2009), Kuopio, Finland (2009)

[14] Immonen, E., Bergström, F., Nurmi, S., Lehtinen, A., Juppi, K., Martinsson, L.: A 2D FSI Model for Paper Webs and Fabrics Moving Close to Each Other in Complex Geometries. Proceedings of the Tenth International Conference on Web Handling (IWEB 2009), Stillwater, Oklahoma (2009)

[15] Juppi, K.: Experimental and Theoretical Study of the Effect of a New Dryer Construction on Paper Machine Runnability. Ph.D. thesis, Helsinki University of Technology (2001)

[16] KnowPap 2008, KnowPap Program 10.0 (11/2008)

[17] Kulachenko, A., Gradin, P., Koivurova, H.: Modeling the dynamical behavior of a paper web. Part II. Computers and Structures, 85:148-157 (2007)

[18] Karlsson, J.: Teoretisk undersökning av torkvirans inverkan på arkladder I en pappermaskin. Master's thesis, Chalmers Tekniska Högskola, Göteborg (1989)

[19] Karlsson, M. (edit.): Papermaking science and technology 9, Papermaking, part 2, drying, Fapet Oy, Helsinki (2000)

[20] Miniature pressure transducer, [www-document] (Unknown place of publication): Kulite Semiconductor Products, Inc., 2009 [Retrieved September 29, 2009]. From: http://www.kulite.com/reference/Handbook/section3.pdf

[21] Kurki, M.: Modeling of Kinematical and Rheological Web Line Behavior in a Papermaking Environment. Licentiate thesis, Lappeenranta University of Technology (2005)

[22] Kurki, M., Martikainen, P.: Adaptive, self –underpressurizing suction roll for fast web handling. Proceedings of the Eight International Conference on Web Handling (IWEB 2005), Stillwater, Oklahoma (2005)

[23] Kurki, M., Åkerholm, J.:Analysis of strongly coupled fluid-structure interaction problem using optimization principle. IX Finish Mechanical Days, Lappeenranta, Finland, 2006

[24] Kurki, M., Martikainen, P., Apr.1, 2008. *Roll in a Paper or Board Machine and a Dryer Group in a Paper or Board machine*. US 7,351,309 B2.

[25] Laakkonen, K.: Method to model dryer fabrics in paper machine scale using small-scale simulations and porous media model. International Journal of Heat and Fluid Flow, 24:114-121 (2003)

[26] Laakkonen, K.: Computational Flow-Field Modeling of Paper Machine Dryer Fabric. Ph.D. thesis, Tampere University of Technology (2003), Publications 414

[27] Laakkonen, K., Kurki, M., Martinsson, L., Toney, M.: CFD Analysis of Dryer Pocket. Tappi Engineering Conference, San Antonio, Texas, (2001). (Cancelled conference in the U.S. due to 11th Sept. 2001)

[28] Lehtinen, A., Bergström, F., Immonen, E., Nurmi, S., Juppi, K. Martinsson, L.: Transient 2D paper web drying model based on CFD. Proceedings of 10th International Conference on Web Handling, Stillwater, Oklahoma USA, 2009.

[29] Leimu, J.: Estimating the Web Behavior in the Opening Nip Area. Professional Papermaking, 1:24-31 (2007)

[30] Leimu, J.: Theoretical and Experimental Investigation of the Cylinder Dryer Opening Nip. Ph.D. thesis, Åbo Akademi University (2008)

[31] DryOnyx Z. [www-document], Updated May 2005 [Retrieved August 13, 2009]. From: http://www.metso.com/MP/Marketing/mpv2store.nsf/BYWID/WID-030117-2256C-0268E/$File/33084_V2_EN.pdf?openElement

[32] Müftü, S., Jagodnik J.: Traction between a web and a smooth roller. Journal of tribology, 126:177-184 (2004)

[33] Müftü, S.: The fluid-structure interaction in supporting a thin flexible cylindrical web with an air cushion. Journal of Fluids and Structures, 13:681-708 (1999)

[34] Müftü, S.: Mechanics of a thin, Flexible, Translating Media and Their Interactions with Surrounding Air. Proceedings of the JSME, Informationm Intelligence & Precision Equipment (IIP) Conference, Tokyo, Japan, 2005.

[35] Müftü, S.: Mechanics of a thin, tensioned shell, wrapped helically around a turn-bar. Journal of Fluids and Structures, 23:767-785 (2007)

[36] Müftü, S., Altan M.: Mechanics of a Porous Web Moving Over a Cylindrical Guide. Journal of Tribology, 122:418-426 (2000)

[37] NI 9229/9239 Specifications. [www-document], [Retrieved October 1, 2009]. From: http://www.ni.com/pdf/products/us/922939ds.pdf

[38] Nurmi, S., Bergström, F., Immonen, E., Lehtinen, A., Juppi, K., and Martinsson, L.: Comparison of aerodynamics between a smooth and grooved roll interacting with a rigid impermeable horizontal wall. Proceedings of Paper Making Research Symposium (PRS 2009), Kuopio, Finland (2009)

[39] Nurmi, S., Bergström, F., Immonen, E., Lehtinen, A., Juppi, K. Martinsson, L.: Modeling grooved rolls with moving 2D porous media. Proceedings of 10th International Conference on Web Handling, Stillwater, Oklahoma USA, 2009.

[40] Nurmi, S., Zamankhan, P., Polashenski, W., Heikkilä, P., Jokioinen, I.: Flotation and Aerodynamic Instability of Webs in a Dryer. ASME Heat Transfer / Fluids Engineering Summer Conference, HT-FED2004-56191. Charlotte, North Carolina, USA: ASME, 2004.

[41] Pakarinen, P., Juppi, K., Karlsson M.: A study of air flows in single-tier pocket at high speed. Proceedings of the 80th annual Meeting of CPPA, Canadian Pulp & Paper Association, Montreal Canada (1995)

[42] Pitkäniemi, T.: Paperikoneen kuivatusosan imutelan virtaukset. Diplomityö, Tampereen teknillinen korkeakoulu, Tampere (2000)

[43] Rice, B., Gans, R.: A simple model to predict web-to-roller traction. Proceedings of the Seventh International Conference on Web Handling (IWEB 2003), Stillwater, Oklahoma (2003)

[44] Sasaki, M., Tanimoto, K., Kohno, K., Takahashi, S., Kometani, H., Hashimoto, H.: In-roll stress analysis considering air-entrainment at the roll-inlet with the effect of grooves on nip roll surface. Journal of Advanced Mechanical Design, Systems, and Manufacturing, 2(1):133-145 (2008)

[45] Sasaki, M., Kohno, K., Tanimoto, K., Takahashi, S., Suzuki, S., Hashimoto, H.: Traction force between rotating rolls and moving web considering the effect of air-entrainment. Microsystems Technology, 13:1161-1167 (2007)

[46] Young, B., Moretti, M.: Interaction of fluttering webs with surrounding air. Tappi Journal, 74:231-236 (1991)

[47] Åkerholm, J.: CFD Simulations in the Dry End of Paper Machines. SIMS 2006. Helsinki, Finland (2006).

[48] Zagar, S.: Computational Fluid Dynamics Helps Solve Web Stability Problem. Pulp & Paper, 74:231-236 (1996)

[49] White, F., Christoph, G.: A Simple New Analysis of Compressible Turbulent Skin Friction Under Arbitrary Conditions. Technical Report AFFDL-TR-70-133, February (1971)

[50] White, F. M., Fluid Mechanics, 4th ed., McGraw-Hill, Boston, 1999, pp.175-176.

[51] Widlund, O., Ragwald, H., Halldin, C., Lindqvist, N.: Aerodynamics of high-speed paper machines. Tappi Journal, 80:113-118 (1997)

[52] Wolfstein, M.: The Velocity and Temperature Distribution of One-Dimensional Flow with Turbulence Augmentation and Pressure Gradient. Int. J. Heat and Mass Transfer, 12:301-318 (1969)

[53] Welp, E., Kleinert, A., Schüler, D.: Prevention of Web Floating at Wrapped Transport and Guide Rollers. Proceedings of the Seventh International Conference on Web Handling (IWEB 2003), Stillwater, Oklahoma (2003)

[54] Welp, E., Kleinert, A., Smukala, V.: Influence of the Gap Throttle Effect on the Winding Process and Roll Quality. Proceedings of the Eight International Conference on Web Handling (IWEB 2005), Stillwater, Oklahoma (2005)

APPENDIX A

Table 5: Test cases for the geometry, velocity and fabric permeability changes.

Case	*r* [mm]	$L_{g,w}$ [mm]	$L_{l,w}$ [mm]	G_f [mm]	$L_{g,h}$ [mm]	*v* [m/min]	*Permeability α* [m/h]	*Wrap angle* [°]	*CFD model*
1 1 0	0.61R	6	6	0.5	20	**1200**	0	180	X
1 2 0	0.61R	**6**	**6**	**0.5**	**20**	**1600**	**0**	**180**	**X**
1 3 0	0.61R	6	6	0.5	20	**2000**	0	180	X
1 1 1	0.61R	6	6	0.5	20	1200	**1800**	180	X
1 2 1	0.61R	6	6	0.5	20	1600	**1800**	180	X
1 3 1	0.61R	6	6	0.5	20	2000	**1800**	180	X
2 1 0	0.61R	6	6	0.5	**10**	1200	0	180	
2 2 0	0.61R	6	6	0.5	**10**	1600	0	180	X
2 3 0	0.61R	6	6	0.5	**10**	2000	0	180	
2 1 1	0.61R	6	6	0.5	**10**	1200	**1800**	180	
2 2 1	0.61R	6	6	0.5	**10**	1600	**1800**	180	X
2 3 1	0.61R	6	6	0.5	**10**	2000	**1800**	180	
3 1 0	0.61R	**4**	6	0.4	20	1200	0	180	
3 2 0	0.61R	**4**	6	0.4	20	1600	0	180	X
3 3 0	0.61R	**4**	6	0.4	20	2000	0	180	
3 1 1	0.61R	**4**	6	0.4	20	1200	**1800**	180	
3 2 1	0.61R	**4**	6	0.4	20	1600	**1800**	180	X
3 3 1	0.61R	**4**	6	0.4	20	2000	**1800**	180	
4 1 0	0.61R	6	**10**	0.375	20	1200	0	180	
4 2 0	0.61R	6	**10**	0.375	20	1600	0	180	X
4 3 0	0.61R	6	**10**	0.375	20	2000	0	180	
4 1 1	0.61R	6	**10**	0.375	20	1200	**1800**	180	
4 2 1	0.61R	6	**10**	0.375	20	1600	**1800**	180	X
4 3 1	0.61R	6	**10**	0.375	20	2000	**1800**	180	

APPENDIX B

Table 6: Test cases for the spiral fabric.

Case	*r [mm]*	$L_{g,w}$ *[mm]*	$L_{l,w}$ *[mm]*	$L_{g,h}$ *[mm]*	G_f *[mm]*	*v [m/min]*	*Permeability α [m/h]*	*Wrap angle [°]*	*CFD model*
5 1 1	0.61R	6	6	20	0.5	1200	**1500**	180	X
5 2 1	0.61R	6	6	20	0.5	1600	**1500**	180	X
5 3 1	0.61R	6	6	20	0.5	2000	**1500**	180	X
6 1 1	0.61R	6	6	20	0.5	1200	**15000**	180	X
6 2 1	0.61R	6	6	20	0.5	1600	**15000**	180	X
6 3 1	0.61R	6	6	20	0.5	2000	**15000**	180	X

Table 7: Test cases for the woven fabric.

Case	*r [mm]*	$L_{g,w}$ *[mm]*	$L_{l,w}$ *[mm]*	$L_{g,h}$ *[mm]*	G_f *[mm]*	*v [m/min]*	*Permeability α [m/h]*	*Wrap angle [°]*	*CFD model*
7 1 1	0.61R	6	6	20	0.5	1200	**1500**	180	X
7 2 1	0.61R	6	6	20	0.5	1600	**1500**	180	X
7 3 1	0.61R	6	6	20	0.5	2000	**1500**	180	X
8 1 1	0.61R	6	6	20	0.5	1200	**8000**	180	X
8 2 1	0.61R	6	6	20	0.5	1600	**8000**	180	X
8 3 1	0.61R	6	6	20	0.5	2000	**8000**	180	X

ACTA UNIVERSITATIS LAPPEENRANTAENSIS

326. SINTONEN, SANNA. Older consumers adopting information and communication technology: Evaluating opportunities for health care applications. 2008. Diss.

327. KUPARINEN, TONI. Reconstruction and analysis of surface variation using photometric stereo. 2008. Diss.

328. SEPPÄNEN, RISTO. Trust in inter-organizational relationships. 2008. Diss.

329. VISKARI, KIRSI. Drivers and barriers of collaboration in the value chain of paperboard-packed consumer goods. 2008. Diss.

330. KOLEHMAINEN, EERO. Process intensification: From optimised flow patterns to microprocess technology. 2008. Diss.

331. KUOSA, MARKKU. Modeling reaction kinetics and mass transfer in ozonation in water solutions. 2008. Diss.

332. KYRKI, ANNA. Offshore sourcing in software development: Case studies of Finnish-Russian cooperation. 2008. Diss.

333. JAFARI, AREZOU. CFD simulation of complex phenomena containing suspensions and flow through porous media. 2008. Diss.

334. KOIVUNIEMI, JOUNI. Managing the front end of innovation in a networked company environment – Combining strategy, processes and systems of innovation. 2008. Diss.

335. KOSONEN, MIIA. Knowledge sharing in virtual communities. 2008. Diss.

336. NIEMI, PETRI. Improving the effectiveness of supply chain development work – an expert role perspective. 2008. Diss.

337. LEPISTÖ-JOHANSSON, PIIA. Making sense of women managers´ identities through the constructions of managerial career and gender. 2009. Diss.

338. HYRKÄS, ELINA. Osaamisen johtaminen Suomen kunnissa. 2009. Diss.

339. LAIHANEN, ANNA-LEENA. Ajopuusta asiantuntijaksi – luottamushenkilöarvioinnin merkitys kunnan johtamisessa ja päätöksenteossa. 2009. Diss.

340. KUKKURAINEN, PAAVO. Fuzzy subgroups, algebraic and topological points of view and complex analysis. 2009. Diss.

341. SÄRKIMÄKI, VILLE. Radio frequency measurement method for detecting bearing currents in induction motors. 2009. Diss.

342. SARANEN, JUHA. Enhancing the efficiency of freight transport by using simulation. 2009. Diss.

343. SALEEM, KASHIF. Essays on pricing of risk and international linkage of Russian stock market. 2009. Diss.

344. HUANG, JIEHUA. Managerial careers in the IT industry: Women in China and in Finland. 2009. Diss.

345. LAMPELA, HANNELE. Inter-organizational learning within and by innovation networks. 2009. Diss.

346. LUORANEN, MIKA. Methods for assessing the sustainability of integrated municipal waste management and energy supply systems. 2009. Diss.

347. KORKEALAAKSO, PASI. Real-time simulation of mobile and industrial machines using the multibody simulation approach. 2009. Diss.

348. UKKO, JUHANI. Managing through measurement: A framework for successful operative level performance measurement. 2009. Diss.

349. JUUTILAINEN, MATTI. Towards open access networks – prototyping with the Lappeenranta model. 2009. Diss.

350. LINTUKANGAS, KATRINA. Supplier relationship management capability in the firm´s global integration. 2009. Diss.

351. TAMPER, JUHA. Water circulations for effective bleaching of high-brightness mechanical pulps. 2009. Diss.

352. JAATINEN, AHTI. Performance improvement of centrifugal compressor stage with pinched geometry or vaned diffuser. 2009. Diss.

353. KOHONEN, JARNO. Advanced chemometric methods: applicability on industrial data. 2009. Diss.

354. DZHANKHOTOV, VALENTIN. Hybrid LC filter for power electronic drivers: theory and implementation. 2009. Diss.

355. ANI, ELISABETA-CRISTINA. Minimization of the experimental workload for the prediction of pollutants propagation in rivers. Mathematical modelling and knowledge re-use. 2009. Diss.

356. RÖYTTÄ, PEKKA. Study of a vapor-compression air-conditioning system for jetliners. 2009. Diss.

357. KÄRKI, TIMO. Factors affecting the usability of aspen (Populus tremula) wood dried at different temperature levels. 2009. Diss.

358. ALKKIOMÄKI, OLLI. Sensor fusion of proprioception, force and vision in estimation and robot control. 2009. Diss.

359. MATIKAINEN, MARKO. Development of beam and plate finite elements based on the absolute nodal coordinate formulation. 2009. Diss.

360. SIROLA, KATRI. Chelating adsorbents in purification of hydrometallurgical solutions. 2009. Diss.

361. HESAMPOUR, MEHRDAD. Treatment of oily wastewater by ultrafiltration: The effect of different operating and solution conditions. 2009. Diss.

362. SALKINOJA, HEIKKI. Optimizing of intelligence level in welding. 2009. Diss.

363. RÖNKKÖNEN, JANI. Continuous multimodal global optimization with differential evolution-based methods. 2009. Diss.

364. LINDQVIST, ANTTI. Engendering group support based foresight for capital intensive manufacturing industries – Case paper and steel industry scenarios by 2018. 2009. Diss.

365. POLESE, GIOVANNI. The detector control systems for the CMS resistive plate chamber at LHC. 2009. Diss.

366. KALENOVA, DIANA. Color and spectral image assessment using novel quality and fidelity techniques. 2009. Diss.

367. JALKALA, ANNE. Customer reference marketing in a business-to-business context. 2009. Diss.